Ozone Monitoring Instrument Calibration

Marcel R. Dobber, Ruud J. Dirksen, Pieternel F. Levelt, G. H. J. van den Oord, Robert H. M. Voors, Quintus Kleipool, Glen Jaross, Matthew Kowalewski, Ernest Hilsenrath, Gilbert W. Leppelmeier, *Member, IEEE*, Johan de Vries, Werner Dierssen, and Nico C. Rozemeijer

***Abstract*—The Ozone Monitoring Instrument (OMI) was launched on July 15, 2004 on the National Aeronautics and Space Administration's Earth Observing System Aura satellite. The OMI instrument is an ultraviolet-visible imaging spectrograph that uses two-dimensional charge-coupled device detectors to register both the spectrum and the swath perpendicular to the flight direction with a 115° wide swath, which enables global daily ground coverage with high spatial resolution. This paper presents the OMI design and discusses the main performance and calibration features and results.**

***Index Terms*—Calibration, charge coupled device (CCD), remote sensing, ultraviolet spectroscopy.**

I. Introduction

THE Ozone Monitoring Instrument (OMI) was launched onboard the Earth Observing System Aura satellite on July 15, 2004. The primary objective of OMI is to obtain global measurements at high spatial and spectral resolution of a number of trace gases in both the troposphere and stratosphere [1]. Using these measurements, science questions on the recovery of the ozone layer, the depletion of ozone at the poles, tropospheric air pollution, and climate change can and will be addressed. Data produced by OMI will continue the long-term global ozone record produced by the National Aeronautics and Space Administration (NASA) Total Ozone Mapping Spectrometer (TOMS) over the past 25 years [2].

Atmospheric constituents are retrieved from nadir observations of backscattered light from the sun on the Earth's atmosphere in the ultraviolet-visible wavelength range (264–504 nm) utilizing differential optical absorption spectroscopy (DOAS) [3], [4] algorithms developed for OMI at the Royal Netherlands Meteorological Institute (KNMI) [5] and algorithms developed for the NASA TOMS instrument [2]. OMI measures the photon flux generated by sunlight either scattered from the Earth's surface and the atmosphere in the radiance mode, or directly from the sun in the irradiance mode via onboard diffusers. The ratio of the calibrated radiance and irradiance equals the Earth atmospheric bidirectional scattering distribution function (BSDF). The ratio of the OMI radiance and irradiance calibration functions equals the BSDF of the instrument, for which the onboard diffuser is the most important contributor. The onboard diffuser transfers (via the diffuser BSDF in 1/sr) the sun irradiance into radiance, which is subsequently measured by the instrument. The ratio of the radiometrically uncalibrated radiance and irradiance signals as measured by the instrument in electrons per second (e/s) equals the ratio of the Earth atmospheric BSDF and the OMI instrument BSDF.

The ozone profile is obtained from the increase in the ozone absorption cross section from 320 to 270 nm. The retrieval methods used for predecessor instruments like the Global Ozone Monitoring Instrument (GOME) on the European Remote Sensing 2 (ERS-2) satellite, the Scanning Imaging Absorption Spectrometer for Atmospheric Cartography (SCIAMACHY) on ENVISAT, TOMS and Solar Backscatter Ultra-Violet (SBUV) will also be applied to OMI measurement data.

In order to meet the science objectives, measurements are needed that combine both a good spatial resolution of 13×24 km^2 and daily global coverage. This is realized by implementation of a unique optical design of the telescope system and the use of CCD detectors, which enables an instantaneous field of view of 115°, corresponding to a 2600-km broad swath on the Earth's surface, while at the same time the desired spatial resolution is obtained. This spatial resolution is required to optimize the probability of observing cloud-free ground pixels, which is important for obtaining the best tropospheric trace gas amounts and to enable OMI to monitor tropospheric pollution phenomena, like biomass burning and industrial pollution, on urban or regional scale. Recording tropospheric pollution is essential for studying human impact on the Earth's atmosphere and climate.

OMI measures the following primary data products: ozone total column, ozone vertical profile, UV-B flux, nitrogen dioxide total column, aerosol optical thickness, effective cloud cover, and cloud top pressure; and the following secondary data products: total column SO_2, BrO, HCHO, and OClO. The effective cloud top pressure is obtained from the Ring effect originating from Raman inelastic scattering at 390–400 nm and from O_2–O_2 absorption at about 465 nm. The cloud cover and (absorbing) aerosol optical thickness are obtained from the broad wavelength dependency of the sun light backscattered

Manuscript received April 29, 2005; revised September 21, 2005. This work was supported in part by The Netherlands Agency for Aerospace Programmes (NIVR) and in part by the National Aeronautics and Space Administration.

M. R. Dobber, P. F. Levelt, G. H. J. van den Oord, R. H. M. Voors, and Q. Kleipool are with the Royal Netherlands Meteorological Institute (KNMI), 3730 AE De Bilt, The Netherlands (e-mail: dobber@knmi.nl).

R. J. Dirksen is with the Royal Netherlands Meteorological Institute (KNMI), 3730 AE De Bilt, The Netherlands and also with Space Research Organization Netherlands, 3584 CA Utrecht, The Netherlands.

G. Jaross and M. Kowalewski are with Science Systems and Applications, Inc., Lanham, MD 20706 USA and also with the NASA Goddard Space Flight Center, Greenbelt, MD USA 20771.

E. Hilsenrath was with NASA Goddard Space Flight Center, Greenbelt, MD 20771 USA. He is now with the Joint Center for Earth Systems Technology, University of Maryland Baltimore County, Baltimore, MD 21250 USA (e-mail: Ernest.Hilsenrath@nasa.gov).

G. W. Leppelmeier is with G&S Associates Oy, 02360 Espoo, Finland (e-mail: gwl@GandS.pp.fi).

J. de Vries is with Dutch Space BV, NL 2303 DB Leiden, The Netherlands.

W. Dierssen and N. C. Rozemeijer are with TriOpSys BV, 3605 JW Maarssen, The Netherlands.

Digital Object Identifier 10.1109/TGRS.2006.869987

from the Earth's atmosphere. By employing a polarization scrambler the instrument is made insensitive to the polarization of the incoming radiances (see Section III-B).

The integration of the OMI proto-flight model (PFM) was completed in 2001 and was followed by an extensive performance verification program, which has shown that the OMI instrument is compliant with all requirements. Subsequently, an extensive on-ground calibration measurement campaign was performed from April–November 2002. During this calibration period measurements on all pertinent topics were performed under both ambient and in-flight representative thermal vacuum conditions. After conclusion of the calibration period the OMI instrument was shipped to the U.S. for integration on the EOS Aura spacecraft. Extensive testing on spacecraft level was performed from November 2002 until March 2004. The satellite with OMI onboard was launched from the Vandenberg Air Force Base on July 15, 2004. After launch a three month check-out and performance verification period was started, called the Launch and Early Operations Phase (LEOP). During this period various special purpose measurements were performed and the performance of the OMI instrument was found to be as expected from prelaunch testing. During the initial four weeks of the mission in orbit, the optical bench and detector temperature was increased to 303 K for optimal outgassing conditions. Subsequently the temperatures were lowered to their operational values. After that the temperature was increased on two more occasions during the LEOP to 303 K for a duration of one week for each occasion. During the LEOP the in-flight calibration was started. The major purposes of the in-flight calibration are: to verify the calibration status of the instrument as based on the prelaunch measurement data and analyses, to investigate if unanticipated in-flight effects occur and to take these into account, and to keep the calibration accuracy of the instrument up-to-date as a function of time, i.e., monitor and correct for potential changes that occur in flight. These purposes make the in-flight calibration a continuous activity until the end of the mission. The anticipated lifetime of the OMI mission is five years.

For remote sensing instruments like OMI a good on-ground calibration delivering reliable calibration key data for 0–1 data processing as well as a good and continuous in-flight calibration are essential to meet the required accuracies of the target scientific data products, especially when the data is to be compared to and to become part of long-term ozone trend records. This is the subject of this paper. In the 0–1 data processing the measured raw instrument data (rows, columns, binary units) is transferred into calibrated physical quantities (viewing angles, wavelengths, (ir)radiances). A complicating factor for the calibration of imaging instruments like OMI is the proper and accurate calibration of the viewing angle dependency. In the sections below several examples describing the complexity originating from the viewing angle dependence are discussed for various calibration parameters, e.g., radiometric calibration, spectral slit function calibration, and calibration of the viewing properties.

OMI has been developed by Dutch and Finnish industry in close collaboration with the climate research and meteorological community and under contract with the Netherlands Agency for Aerospace Programmes (NIVR) and the Finnish Meteorological Institute (FMI). The Royal Netherlands Meteorological Institute (KNMI) is the Principal Investigator (PI) institute for the OMI instrument. The international OMI science team has approximately 100 members.

TABLE I
OMI INSTRUMENT PROPERTIES

Spectral range	UV1: 264-311 nm UV2: 307-383 nm VIS: 349 – 504 nm
Spectral sampling	UV1: 0.33 nm / px UV2: 0.14 nm / px VIS: 0.21 nm / px
Spectral resolution (FWHM)	UV1: 1.9 px = 0.63 nm UV2: 3.0 px = 0.42 nm VIS: 3.0 px = 0.63 nm
Telescope swath IFOV	115 degrees (2600 km on the ground)
Telescope flight IFOV	1.0 degrees (12 km on the ground)
Ground pixel size at nadir, global mode (electronic binning factor 8)	UV1: 13 km x 48 km UV2: 13 km x 24 km VIS: 13 km x 24 km
Ground pixel size at nadir, spatial zoom-in mode (electronic binning factor 4)	UV1: 13 km x 24 km UV2: 13 km x 12 km VIS: 13 km x 12 km
Silicon CCD detectors	780 x 576 (spectral x spatial) pixels
CCD detector shielding	10 kg, about 29 mm thick aluminum
Operational CCD temperature	UV: 265.07 K VIS: 264.99 K
In-orbit CCD temperature excursion	UV and VIS: ±10 mK (stabilized)
Operational optical bench temperature	264 K
In-orbit optical bench temperature excursion	±300 mK
Duty cycle	60 minutes on daylight side (Earth and sun measurements) 10-30 minutes on eclipse side (calibration measurements)
Average data rate	0.8 Mbps
Power	66 W
Mass	65 kg
Size	50 cm x 40 cm x 35 cm
Orbit	Polar, sun-synchronous Average altitude: 705 km (438 mi) Orbit period: 98 minutes 53 seconds Ascending node local time: 1:42 PM

II. General Description of the Instrument

For the OMI instrument the following subsystems can be identified. The optical bench is the heart of the instrument. The two CCD detectors located in the two detector modules, which are in turn located on the optical bench, produce the recorded spectra and transfer these via a video line to a separate electronics and instrument control unit, the electronics unit (ELU), which digitizes the measured signals. The ELU transfers the measurement data and exchanges the instrument commands to and from the instrument on one hand and to and from the so-called Interface Adapter Module (IAM) on the other hand. The latter forms the interface between the OMI systems and the EOS Aura spacecraft. In flight the optical bench is operated at 264 K. The cooling is realized by a passive radiator plate with dimensions of about 40 cm $\times$ 30 cm. Without additional heating the optical bench cools down to about 255 K in flight. Four passive heaters warm the optical bench to its operational temperature of 264 K. The four heaters have capacities of respectively 1, 2, 4, 8 W, i.e., in total 15 W of heater power is available. In order to obtain an optical bench temperature of 264 K 10 W of heater power are required. The optical bench temperature changes by about 1° for 1 W of heater power. The

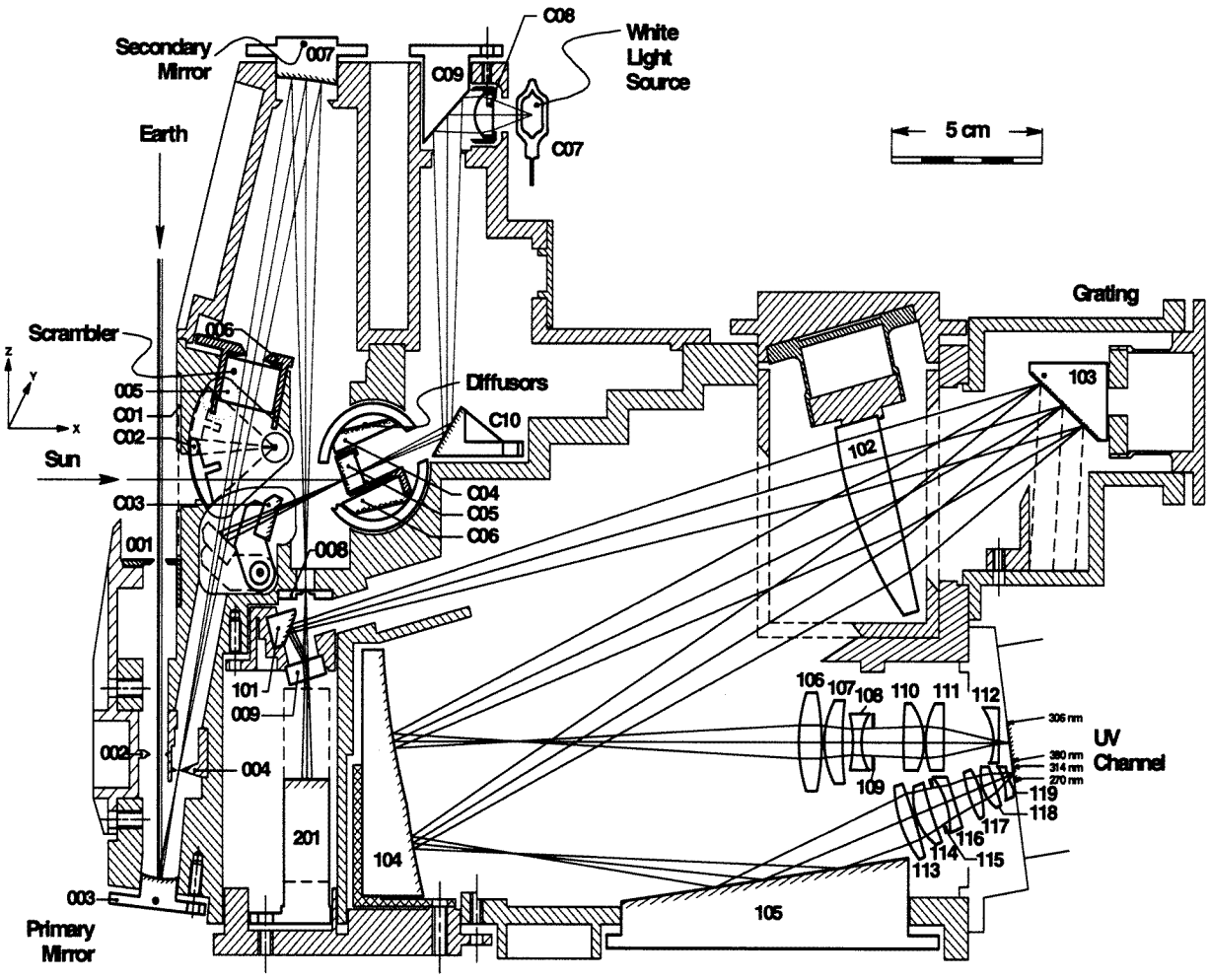

Fig. 1. Optical layout of the OMI telescope, ultraviolet (UV1, UV2) channels, sun path, and calibration optics. The component numbers are referred to in the text.

CCD detectors are warmed up to their operational temperatures of about 265 K with separate active heaters. This is done in a closed-loop feedback system, with which an in-flight temperature stability of about 10 mK is obtained. Tests prior to launch revealed the necessity of protecting the CCD detectors from the in-flight particle environment. After careful analysis, 10 kg of additional aluminum shielding with average thickness of about 29 mm was placed all around the CCD detectors. Table I summarizes a number of important OMI instrument and system properties. The optical bench, detector modules and electronics unit are described in detail in the following sections. More details can be found elsewhere [6]–[9]. The operational 0–1 data processing algorithms and in-flight operational aspects are discussed in [10].

III. Optical Description of the Instrument

The optical layout of the instrument is shown in Figs. 1 and 2 for the ultraviolet and visible channels, respectively. The Earth radiance enters the telescope, which consists of two bare aluminum spherical mirrors (003 and 007), and is imaged on the 44-mm long and 300-μm broad entrance slit (008). The telescope is of a special design that provides an instantaneous field of view of 0.8° in the flight-direction (along-track) and of 115° in the swath direction (cross-track). Combined with a number of other instrument characteristics, which will be discussed below, these fields of view yield an overall ground coverage of about 15 km (along track) by 2600 km (across track) at an altitude of 700 km. This is sufficient to provide daily global coverage of the Earth, at all latitudes. The cross-track resolution is either 24 km (global mode) or 12 km (spatial zoom-in mode) at nadir, depending on the electronics settings. The operational details of the detectors and the electronics are discussed in detail in Section IV.

A polarization scrambler is located in the vicinity of the aperture stop 006 of the telescope. The OMI polarization behavior and the operation of the polarization scrambler are explained in detail in Section III-B. Behind the entrance slit 008 a dichroic mirror 009 reflects the ultraviolet part of the spectrum to the

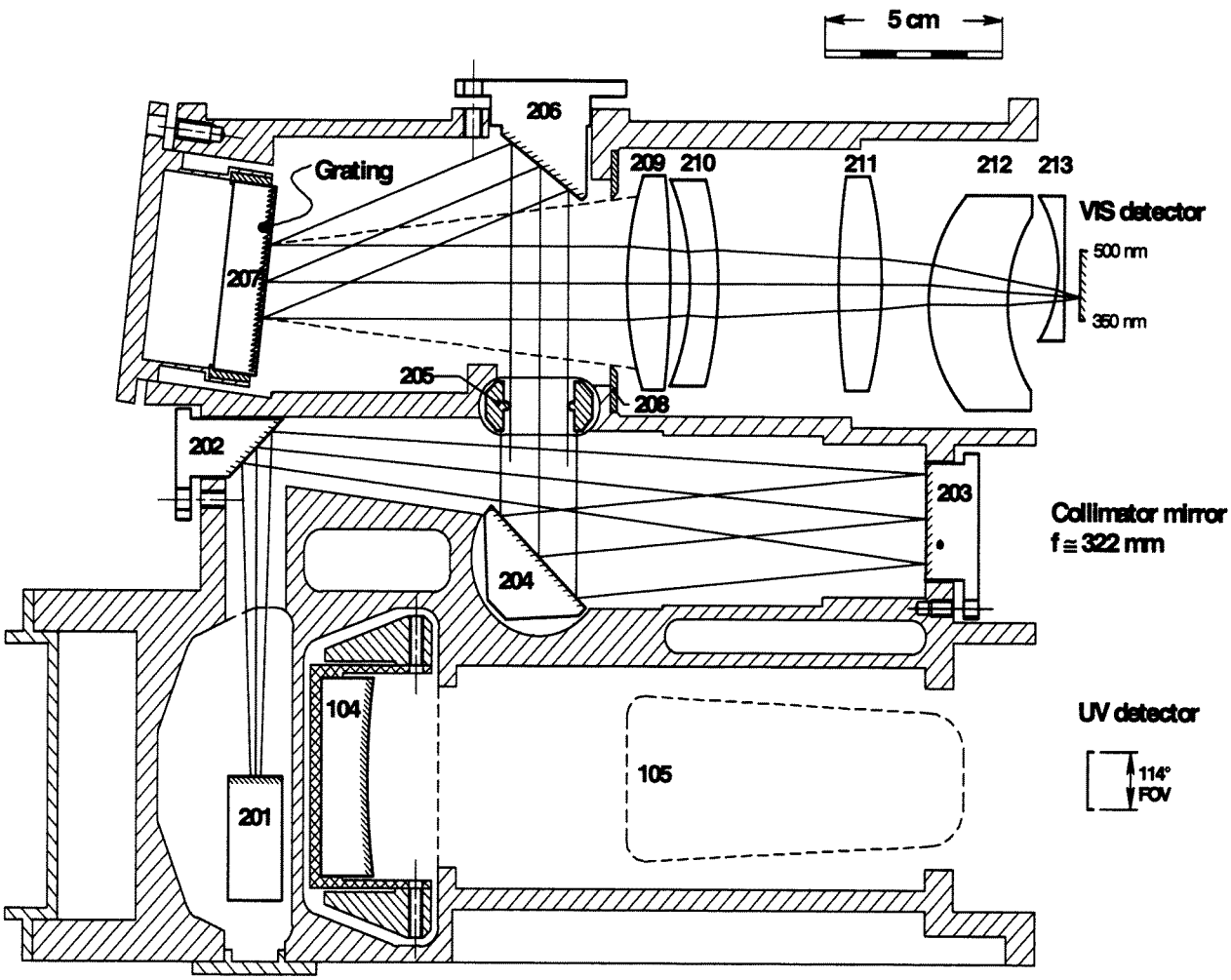

Fig. 2. Optical layout of the OMI visible channel. The component numbers are referred to in the text.

UV channel (264–383 nm) and transmits the visible part of the spectrum to the VIS channel (349–504 nm). The dichroic mirror characteristics define the UV-VIS overlap region, which is about 30 nm wide. The backside of the dichroic mirror is antireflection coated for the visible wavelength range.

Folding mirror 101 reflects the light to the fused-silica field-lens 102 in the UV channel. Final dispersion in the UV channel is achieved by the blazed-holographical grating 103 (2880 lines per mm, blaze angle 28°), that is used in first order. Field lens 102 collimates the incident beam toward the grating and creates an intermediate spectrum near field mirror 104. This field mirror reimages the system pupil stop at 006 at components 115 of the UV1 and 109 of the UV2 imaging objectives. Mirror 104 consists of two spherical concave mirrors that reflect the UV1 wavelength range (264–311 nm) and the UV2 wavelength range (307–383 nm) toward the UV1 objective 113–119 and the UV2 objective 106–112, respectively. Thus, field mirror 104 splits the ultraviolet wavelength range into two channels (UV1 and UV2) and provides the channel overlap between these two channels. Since the intermediate UV spectrum is located just in front of the field mirror 104 rather than on its surface, a small gradual spectral overlap between UV1 and UV2 is obtained. Field mirror 104 has a coating with a wavelength (position on the mirror) dependent variable reflection. For the lower part of the mirror, which reflects the lower wavelength range of the spectrum, the higher wavelengths and thus the spectral stray light are suppressed considerably, typically by one order of magnitude. Both ultraviolet channels are finally imaged onto the same CCD detector. The UV1 channel is reflected via the large bare aluminum folding mirror 105 at large incidence. As a result the UV1 spectrum is reversed on the CCD detector as compared to the UV2 spectrum. The ultraviolet channel is split in two channels in order to cope with the large dynamic range of the Earth input spectrum and for optimal spectral stray light suppression. For signal-to-noise reasons the UV1 channel is imaged by the channel objective in the spatial dimension onto half of the CCD area as compared to the UV2 channel, which is imaged optimally in spatial dimension onto the available CCD area by its objective. The spectral dimension is imaged on the CCD dimension that has 780 pixels (columns), while the spatial dimension (viewing direction) is imaged on the CCD dimension that has 576 pixels (rows).

After the dichroic mirror the visible beam is reflected at 90° by flat mirror 201 toward the VIS channel. Folding mirror 202, collimating mirror 203 and folding mirrors 204 and 206 (all

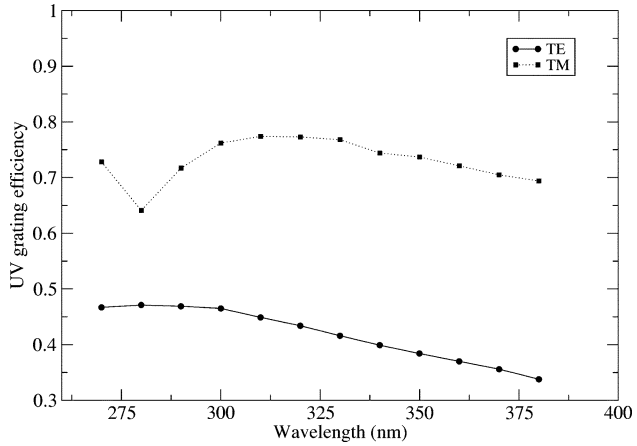

Fig. 3. Polarization-dependent grating efficiencies for the UV channel grating.

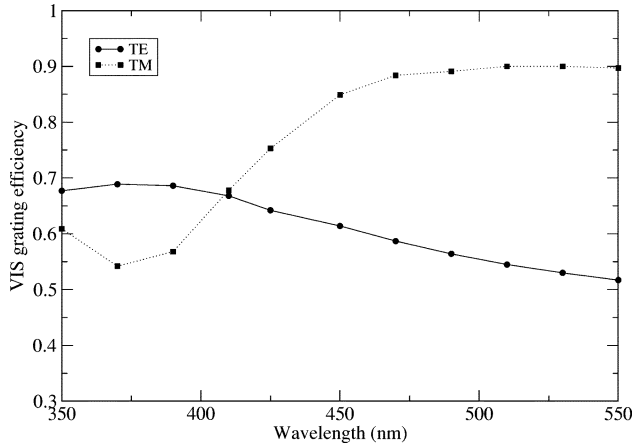

Fig. 4. Polarization-dependent grating efficiencies for the VIS channel grating.

MgF_2 coated aluminum) direct the beam toward the blazed holographical grating 207 (1350 lines per mm, blaze angle 17°). The channel objective (209–213) images the beam onto the visible CCD detector. The gratings are particularly important for the spectral stability of the instrument. The UV and VIS grating efficiencies for both polarization directions are shown in Figs. 3 and 4.

The sun spectrum is used to normalize the Earth spectra in order to obtain the absolute Earth reflectance spectra and to perform accurate wavelength calibrations. OMI observes the sun via optical mesh C01 by opening the solar aperture mechanism C02. The mesh has a transmission of 10% and has many rectangular slits of about 450-μm width and about 20-μm height. The mesh design avoids edge effects and the slit sizes are sufficiently large to avoid diffraction in the OMI wavelength range. The slits are positioned in the mesh in such a way that shadowing effects on the onboard diffusers are avoided. The sun irradiance directly illuminates one of three onboard reflectance diffusers located on diffuser carrousel: only two are shown in Fig. 1: C04 and C06. The diffusers are 40 mm in length and 16 mm in width. The reverse image of the OMI entrance slit on the diffusers is banana-shaped and has dimensions of about 28 mm $\times$ 8 mm. Light from the diffusers illuminates the uncoated bare concave folding mirror C03, which is located on a folding mirror mechanism. This mechanism has two positions: the Earth position, which lets the light from the primary telescope mirror 003 through to the scrambler 005, and the sun position, which not only directs the sun light from the diffusers via C03 to the scrambler 005, but also blocks the Earth radiance from primary telescope mirror 003. The mirror curvature of C03 is intended to replace for the sun mode the telescope function of the primary telescope mirror 003 in the Earth mode. In this way, the telescope properties are designed to be the same for the Earth radiance and the sun irradiance modes. Thus, the difference between the radiance and irradiance modes is the primary telescope mirror 003 in the former mode and the reflection diffusers and folding mirror C03 in the latter mode. The ratio of the two optical paths, being the ratio of the radiance and irradiance radiometric calibrations, is called the instrument bi-directional scattering distribution function (BSDF). This calibration parameter basically describes the Earth reflectance calibration of the OMI instrument, which will be discussed in more detail in Section V-A.

Even though the folding mirror C03 is designed to replace for the irradiance mode the primary telescope mirror 003 for the radiance mode the telescope properties of both modes are not completely identical. From a radiometric calibration point of view this presents no problems, since both modes were radiometrically calibrated accurately prior to launch (see Section V). The purpose of the curved folding mirror in the irradiance mode is to ensure that the reflected light from the diffuser illuminates the spectrometer's entrance slit 008 in combination with the secondary telescope mirror 007. This is similar to the way the primary and secondary telescope mirrors 003 and 007 illuminate the spectrometer's entrance slit 008 in the radiance mode. Thus, for every viewing angle in the radiance mode a reference irradiance spectrum at an optically corresponding viewing angle is available.

The reflection diffusers are used close to the specular angle in the short dimension with an angle of incidence of 11°. In this plane the angle of incidence varies in flight with the orbit position during a sun observation sequence of 154 s. During this time the elevation angle on the diffuser changes from about $11 + 4 = 15°$ to $11 - 4 = 7°$. The OMI-defined elevation angle changes from $+4$ to $-4°$. In the dimension corresponding to the length of the diffusers the incidence angle is nominally about 26°, corresponding to the 1:40 P.M. ascending node time of the EOS Aura orbit. This incidence angle varies as a function of season from about $26 - 5 = 21°$ to $26 + 5 = 31°$. The angle from the diffuser to C03 is perpendicular. The diffusers and their optical properties are further discussed in detail below in Sections III-C and V-D.

The entrance slit 008 of the spectrometer determines a number of spectral, radiometric, and viewing properties of the instrument. The length of 44 mm corresponds to the cross-track viewing swath of 115°, while the width of the slit determines the 0.8° instantaneous field of view in the flight direction (telescope property) and the spectral resolution of the instrument, together with the remaining channel optics (total instrument property). The slit width is not completely constant along the length of the slit: slit width irregularities up to 10 μm are observed under the microscope. These variations in slit width are imaged by the spectrometer into wavelength-independent radiometric variations of several percent as a function of viewing

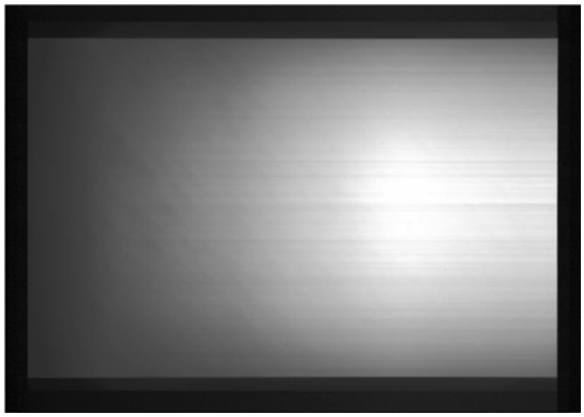

Fig. 5. Horizontal stripes, dependent on viewing direction and independent of wavelength, in the VIS channel as observed in a white light source measurement. These features originate from irregularities in the entrance slit width.

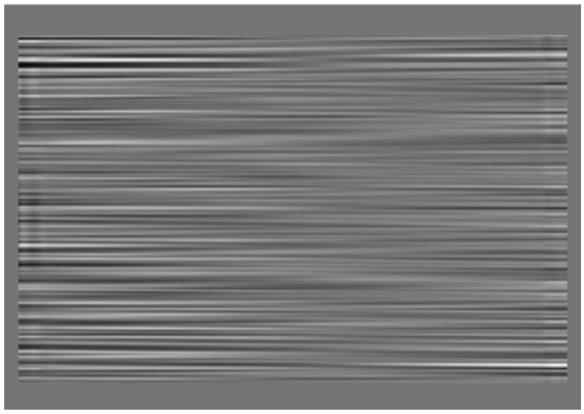

Fig. 6. Diffuser features of the onboard transmission diffuser C05 as observed with the internal white light source in the VIS channel. The spectral dimension is horizontal, the viewing direction dimension vertical. The features are nearly horizontal, but do vary slightly with wavelength.

direction, i.e., horizontal stripes on the images as observed on the CCD detectors. The effect, shown in Fig. 5, is not expected to change in flight and can be characterized and corrected for.

OMI is equipped with a quartz tungsten halogen white light source (WLS) C07 (5 W, 12 V). The light is imaged via lens C08 and mirrors C09 and C10 onto a transmission diffuser C05 located in the diffuser carrousel. Thus, the diffuser carrousel has four positions: three for the reflection diffusers used in the solar modes and one for the transmission diffuser used for the WLS. In order to observe the WLS, the folding mirror mechanism with mirror C03 needs to be placed in the calibration setting as for the solar observations. This setting blocks the Earth view. The transmission diffuser is ground on the first surface, the back surface is polished. The purpose of the WLS is threefold. First and most importantly, the WLS allows for detailed monitoring of the CCD detector properties, because it provides a smooth illumination in both the spectral and the spatial dimension. By analyzing the WLS measurements, the pixel-to-pixel response nonuniformity (PRNU), an important detector calibration parameter (Section XI), can be determined in flight. The PRNU analysis is complicated by two additional effects: the entrance slit irregularities that produce the horizontal stripes on the CCD as described above and, second, spectral and spatial features originating from the transmission diffuser. These features show up on the CCDs as nearly horizontal stripes, as shown in Fig. 6. Both effects need to be taken into account when calculating the PRNU from WLS measurement data. The origin of the transmission diffuser features is explained in Section III-C. The WLS can also be used to monitor in relative sense the radiometric throughput of the instrument, provided that there are independent verifications to distinguish optical throughput degradation from lamp degradation. The lamp is radiometrically stable and reproducible to an accuracy of typically 1%. It is known for this type of lamp that zero-gravity causes the ultraviolet output of the lamp to increase by as much as 65% at 270 nm. Fig. 7 shows a comparison of OMI WLS measurements performed on the ground and in flight. The results are in line with the results obtained for the SCIAMACHY instrument on the European Space Agency's ENVISAT satellite, which uses a similar lamp. The increase in lamp output is caused by changes in the halogen cycle within the lamp as a result from the absence of gravity in space.

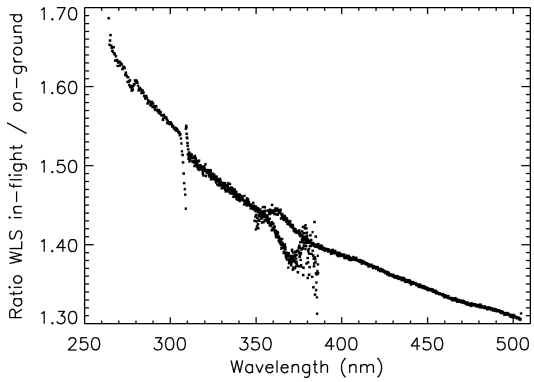

Fig. 7. Ratio WLS output in-flight/on-ground. The output flux is at 270 nm about 65% higher in-flight than on-ground as a result of the absence of gravity, which influences the halogen cycle in the lamp.

The WLS is measured in flight once per week. The thermal behavior of the lamp has no noticeable impact on the instrument in flight.

For on-ground calibration purposes it was also possible to replace the white light source C07 by dedicated optics. This has the advantage that the complete entrance slit 008 is filled homogeneously and thus that the complete CCDs are illuminated. This is also possible via the irradiance mode, but in that case the onboard diffusers and the solar mesh reduce the light flux considerably. The illumination via the white light source path is called the calibration port illumination in the remainder of this document. The calibration port illumination adds to the radiance and irradiance illumination ports discussed above. Obviously the calibration port is not used for absolute radiometric measurements, for which it is important that the employed optical path is exactly the same as used in flight for the radiance and irradiance optical ports. The calibration port is ideal for performing wavelength calibration, spectral slit function, spectral stray light and reference gas cell absorption measurements.

Both the UV and VIS channel are equipped with two green LEDs, which are located directly in front of the CCD detectors. These LEDs can be used to monitor the CCD pixel behavior at 500 nm, which is not fully representative for all wavelengths that fall onto the CCD detectors, but at least gives a good idea on the CCD performance on individual pixel resolution. The two

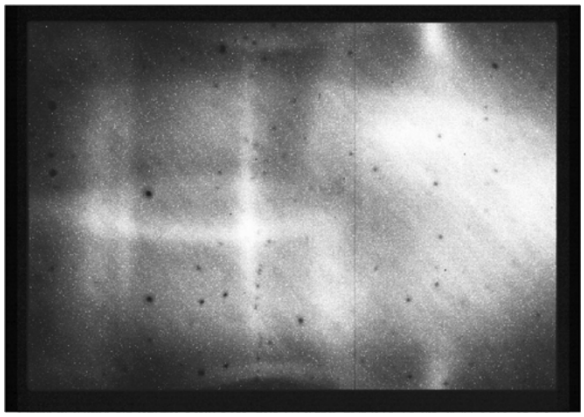

Fig. 8. Unbinned LED measurement in the VIS channel, showing inhomogeneities originating from the LEDs and direct CCD illumination. The spectral dimension is horizontal, the viewing direction dimension vertical, but the illumination is close to monochromatic at about 500 nm, because the LEDs are located directly in front of the detector.

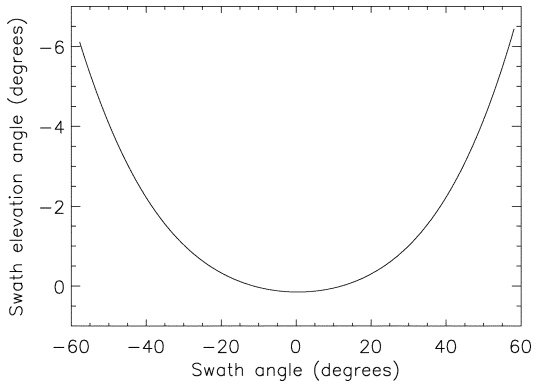

Fig. 9. Telescope elevation angle as a function of swath angle for column 300 in the UV2 channel.

LEDs in the VIS channel illuminate the CCD detector directly via the channel objective, whereas the illumination of the UV CCD detector by the two LEDs in that channel is indirect. This difference in illumination characteristics causes a structure in the LED measurements in the VIS channel, which is absent in the UV channel. The effect, which manifests itself as multiple small areas in the CCD image with about 10% reduced efficiency, is tentatively attributed to inhomogeneities in the LED itself, which are imaged onto the CCD detector surface. A representative example of the effect is shown in Fig. 8. The LED measurements are operationally performed once per day in orbit.

By using the various calibration options in flight, the optical degradation behavior can be traced back to specific parts of the total optical system, e.g., diffusers, C03, WLS, detector. However, the primary telescope mirror 003, used for the Earth radiance observations only, is excluded from these comparisons. In the optical design as well as by in flight operations every possibility to minimize optical degradation of this mirror has been applied. During the first four weeks in orbit the optical bench and CCD detector temperatures were raised to 303 K in order to realize optimal outgassing conditions in this crucial first phase of the mission. In addition, during the first three months of operation in space, the temperatures were increased to 303 K twice for various days to provoke further outgassing and to characterize the performance of the instrument at 303 K. Finally, mirror 003 is carefully stowed away inside the instrument behind a small aperture 002 (area about 1 cm^2), preventing in orbit contaminants from reaching this mirror too easily (aperture 002 also serves the purpose of reducing spatial stray light). Even though the primary telescope mirror 003 is not expected to degrade considerably, it is planned to monitor the temporal efficiency of the radiance optical path by comparing the radiance levels from a number of well-defined ground scenes, e.g., ice sheets of Greenland or the Antarctic.

A. Telescope

The telescope of the OMI instrument consists of the primary mirror 003 and the secondary mirror 007, with the polarization scrambler 005 and the system aperture stop 006 placed in between. By placing the system pupil stop 006 in the focal plane of the secondary mirror 007, the swath direction field of view of 115° is made telecentric for the output beams of the telescope. Thus, the various viewing directions of the 115° instantaneous field of view are imaged on different locations in the length of the entrance slit. This explains why any irregularities in the slit width over its length are imaged onto the CCDs as swath viewing angle dependent radiometric attenuations, i.e., horizontal and wavelength-independent stripes. The angle of 115° between the extreme angles is reduced to about 30° at the position of the polarization scrambler. Spatial stray light and optical degradation as a result of exposure is reduced by placing an oversized aperture 002 in front of the primary telescope mirror. In the focal plane of the primary mirror an oversized slit 004 is positioned, also to reduce stray light. The system pupil stop 006 has dimensions 7.6 mm in the swath dimension and 5.6 mm perpendicular to the swath dimension. The instrument has an F-number of F/15 in the flight direction and F/11 in the swath direction. The focal length of the telescope in the nadir direction is 21.73 mm. This yields a light collecting area of the telescope for nadir measurements of 2.6 mm^2, which is the size of the aperture stop of the telescope. The telescope system itself has an F-number of F/1.5, F/3.2, and F/5.0 for the UV1, UV2, and VIS channels, respectively.

The secondary telescope mirror 007 has a special coating with a reflection of 20% at 500 nm (decreasing to 8% at 750 nm) in order to reduce the light intensity to the visible channel and to suppress stray light from wavelengths above 500 nm. In this way the apertures in the instrument could be increased to provide optimal polarization scrambler performance in terms of spectral features (see Section III-B). The telescope has a field of view in the flight direction of about 0.81°, which is increased by the polarization scrambler to about 1.00° (see Section III-B). In the swath dimension the field of view is about 115°. As the swath angle is increased toward 57°, the viewing elevation direction of the telescope in the flight dimension changes by about 6°. For larger swath angles the instrument is looking more backward on the ground as compared to the nadir view (swath angle 0°). This dependence is shown in Fig. 9.

The spatial stray light performance of the telescope was also measured. For 1° to 2° off-specular angles the signal was observed to be three to four orders of magnitude smaller than for the specular angle.

B. Polarization Scrambler

Nearly all of optical components used in the OMI optical design have reflective or transmissive properties that are to some degree dependent on the polarization state of the incident light. This is especially true for the channel separation dichroic mirror 009 and the UV grating 103 and the VIS grating 207, for which the polarization-dependent efficiencies were shown in Figs. 3 and 4. In general, instruments with gratings such as OMI can be up to two to three times more radiometrically sensitive to one state of linear polarization than the perpendicular counterpart (parallel to entrance slit 008 versus perpendicular to entrance slit). There are two possibilities to deal with the polarization dependency of the radiometric calibration. The first one is to determine the polarization state of the incident light, i.e., the degree and direction of polarization, in order to correct for it. This is the approach used in instruments such as GOME (ERS-2) and SCIAMACHY (ENVISAT). In this approach the on-ground calibration and 0–1 data processing become more elaborate and the resulting radiometric inaccuracies are generally increased as compared to the unpolarized case. The alternative approach, which is employed in the OMI instrument and heritage NASA ozone sensors, is to use a polarization scrambling device to make the instrument insensitive to the incident polarization state. The OMI polarization scrambler 005 is positioned between the two telescope mirrors 003 and 007. This makes the instrument and its calibration conceptually more simple, but the scrambler has a number of properties that must be considered carefully for the application in OMI.

The type of polarization scrambler employed in OMI is a spatial pseudodepolarizer. A wedge (about 6°) of birefringent quartz introduces a continuous phase difference between the ordinary and the extraordinary beams. Behind the wedge all possible polarization states are present as a function of position in the extended beam. A second opposite wedge with its optical axis orientated perpendicularly to the first one compensates for beam deviating and refraction effects, whilst maintaining the polarization changes of the first wedge. With such a configuration linearly polarized light parallel or perpendicular to the optical axis pass the double wedge unchanged. To cover all incident polarization states a second pair of wedges is added after the first one at an optical axis orientation of 45° with respect to the optical axis of the first pair. The resulting device is called a Dual Babinet Compensator Pseudo-depolarizer (DBCP).

There are two optical properties of the polarization scrambler described above that need to be considered carefully: spectral features and beam separation. A theoretical optical model has been developed to describe the radiometric response properties of the scrambler. This model, based on a Mueller matrix approach, will not be described in detail here. An important parameter for both the model and the actual performance of the scrambler is the shape of the aperture stop per optical channel. The channel-dependent aperture determines the magnitude of the spectral features originating from the scrambler: the larger the aperture, the smaller the feature amplitude. For UV1 and UV2 the aperture stop is determined by aperture stop 006, just behind the scrambler. For the VIS channel the effective aperture stop is determined by 205. Simulations and measurements show that the scrambler introduces sinusoidal radiometric features as a function of wavelength with typical amplitudes of 0.01%. The wavelength period as well as the amplitude increase with wavelength. These features interfere detrimentally with the Earth atmosphere retrieval techniques that use the high spectral resolution of the OMI instrument, such as DOAS. It is therefore important to minimize the amplitude of these features. The larger the area of the scrambler as seen by the CCD detector pixels is, the smaller the residual spectral features will be. The shape of the aperture stops per channel also influences the final spectral feature performance: soft rims on the apertures decrease the amplitudes of the spectral features. The scrambler feature performance also changes with angle of incidence, which varies between $-15°$ and $+15°$ at the position of the scrambler 005 in the telescope system. Basically, the pattern shifts with wavelength as a function of the incidence angle.

Taking all parameters into account the theoretical model predicts a remaining polarization scrambler spectral feature amplitude of less than $5 \cdot 10^{-5}$ in UV1 and less than $2 \cdot 10^{-4}$ in VIS channel. These amplitudes, as well as the wavelength periods of typically 10 nm at 280 nm and 35 nm at 480 nm, have been verified qualitatively and quantitatively on scrambler component level using a dedicated measurement setup. A verification was also performed on integrated instrument level, which proved to be quite difficult, because the experimental setup itself easily introduces spectral features in the order of 10^{-4}. This verification confirmed that the scrambler spectral features were below $2 \cdot 10^{-4}$ in the UV2 channel and below $5 \cdot 10^{-4}$ in the VIS channel.

The polarization scrambler also separates the incoming beam into four separate outgoing beams, oriented in a parallelogram. The underlying optical principle of the beam separation is the same as in a Wollaston prism. The four beams are separated by about 0.4° in object space and divide the energy of an unpolarized incident beam equally. The exit beams are fully linearly polarized (in two pairs of perpendicular states), which has been verified experimentally using a polarized HeNe laser and an analyzer. The scrambler thus deteriorates the optical performance of the telescope system. Backtracing from the CCD pixels, one could say that the instrument looks at four slightly shifted ground scene pixels. As described above the instantaneous field of view of the bare telescope (without scrambler) amounts to about 0.81°. The scrambler increases this number to about 1.00°, corresponding to about 12 km at 700-km altitude. This number has been confirmed experimentally on the integrated instrument by measurements on the viewing properties (see Section VI).

The incident polarization sensitivity of the OMI instrument as a whole is determined by the polarization-dependent reflective properties of the first telescope mirror 003, the first surface of the polarization scrambler 005, and the characteristics of the polarization scrambler itself. The first surface of the polarization scrambler is left uncoated in order to compensate as much as possible for the polarization-dependent reflectance of the first telescope mirror 003. The remaining three surfaces of the scrambler are antireflection coated (optimized at 290 nm) with MgF_2 layers to improve the transmission characteristics as much as possible and to reduce internal reflections as much as possible. Theoretical models that account for the polarization properties of the first telescope mirror and the first surface of the scram-

bler show that this system is polarization-independent to 0.4%, i.e., the instrument response is the same to 0.4% whatever polarization state of the incident light is offered. This has been verified experimentally, both on component level for the telescope components as well as on integrated instrument level. For the latter verification a white light source illuminating a spectralon plate and a Glan–Thompson polarizer in alternately horizontal and vertical polarization orientation have been used. The measured polarization sensitivity was 0.4% for the UV1 channel, which has the highest signal, and about 1% for the UV2 and VIS channels, which is attributed to the accuracy of the experimental setup.

C. Reflection Diffusers and Diffuser Spectral and Spatial Features

OMI is equipped with two ground aluminum diffusers (thickness 4 mm) and one volume diffuser, which consists of 6-mm-thick quartz ground on both sides and coated with aluminum on the backside. The aluminum diffusers are used mainly for radiometric calibration purposes: one is observed once per week and the other once per month in order to enable monitoring of optical degradation behavior in space. The volume diffuser is observed once per day. The different observational frequencies for the three reflectance diffusers allow for an accurate monitoring of exposure-dependent optical degradation. Besides its use for radiometric calibration, the volume diffuser has proven to provide the best solar reference spectrum because diffuser-induced spectral and spatial features are considerably (at least one order of magnitude) smaller than for the aluminum diffusers. These features are thought to arise from interference effects from the diffuser surface. The sun spectra are used to normalize the Earth radiance spectra in order to obtain the absolute Earth reflectance spectra. These in turn are used to retrieve information about the Earth's atmosphere, so uncharacterized spectral features affect products in the same way as is the case for the spectral features introduced by the polarization scrambler 005. The features introduced by the onboard diffuser employed to measure the daily reference spectrum interfere detrimentally with the Earth atmosphere retrieval techniques that make use of the high spectral resolution of the OMI instrument, such as DOAS. The polarization scrambler features cancel in first order in the Earth reflectance, because they are similar in both the radiance and irradiance optical paths of the instrument. Such is not the case for the diffuser features, which appear only in the irradiance optical path. These too would have little effect on measured Earth reflectance if they were properly characterized. However, it is nearly impossible to adequately characterize how these features vary with solar illumination.

The origin of the observed diffuser features can be found in the location of the diffusers in the optical system: they are located very close to a focal point of the instrument telescope. The area observed on the diffusers per CCD detector viewing direction is only 1–2 mm^2. The surface structure of the diffusers is therefore basically imaged onto the CCD detectors, where it shows up as spectral and spatial nonuniformity in the observed signals. This mechanism also applies to the transmission diffuser C05, which is used for the WLS observations. For the volume diffuser light is mainly scattered in a forward direction by the first roughened quartz surface, then travels through 6 mm of quartz before being reflectively scattered on the back-surface of the diffuser. The outgoing beam is traveling back through the quartz and scattered in the forward direction once more by the first diffuser surface. Thus, the OMI instrument sees considerably less structure for the volume diffuser than for the aluminum diffusers, which have only one roughened reflective surface with granular surface finish. This explains why considerably less spectral and spatial structure is observed via the volume diffuser. Further details on the appearance of the diffuser features are given in Section V-D.

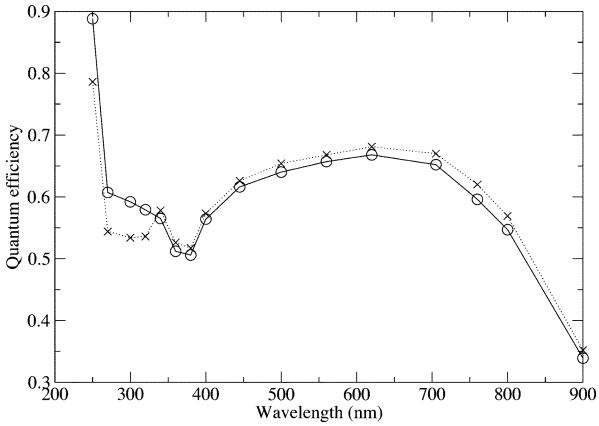

Fig. 10. Quantum efficiency for UV (circle) and VIS (crosses) CCD detectors.

IV. Description of Instrument Electronics and Detectors

The OMI detector system is divided up into two parts: the detector modules (DEMs) containing the CCD detector and the ELU that controls the DEMs. Each spectral channel (UV & VIS) is equipped with its own DEM. The ELU commands the DEMs in all its aspects and samples the DEM signals. The ELU takes care of all communication toward and from the CCD detectors. The ELU offers a variety of possibilities for operating the DEMs. In the discussion below we will confine ourselves to the relevant in-flight modes only. First, the operational principles of the DEM and the ELU are discussed. Subsequently, more detailed operational information is presented and discussed.

A. Detector Modules

The detector modules consist of a backilluminated, UV-enhanced silicon based CCDs, plus basic readout electronics. The detectors are manufactured by depositing the silicon detector material on a carrier substrate. Subsequently the detector is turned over and the carrier material is etched away, leaving the bare silicon detector material on top. This etching process is responsible for the pixel response nonuniformity (see Section XI). Finally, an ultraviolet antireflection coating is deposited on the silicon material. This coating increases the detector UV quantum efficiency at 270 nm by about 30%. The quantum efficiencies for the UV and VIS CCD detectors used in OMI are shown in Fig. 10.

The CCD consists of three regions: an image region, a storage region and a readout region. This allows the CCD to be operated

TABLE II
ELECTRONICS PARAMETERS FOR THE UV AND VIS CHANNELS. THE ELECTRONICS CONVERSION FACTORS ARE 618.203 AND 612.803 ELECTRONS PER BINARY UNIT FOR THE UV AND VIS CHANNELS, RESPECTIVELY. THE FULL ADC RANGE IS 12 bits

Gain code	Relative gain	Offset [ADC counts]	Readout noise [electrons]
UV 0	11.514	435.9	42.3
UV 1	38.318	1346.2	33.2
UV 2	1.000	102.0	313.8
UV 3	3.3274	173.3	99.8
VIS 0	11.453	376.5	43.8
VIS 1	38.168	1059.7	29.7
VIS 2	1.000	102.4	239.4
VIS 3	3.3193	166.6	88.5

in frame transfer mode, in which the image is rapidly (4.32 ms) transferred from the light sensitive image region to the masked storage region after illumination. The image is read-out from the storage region while the exposure of the next image starts in the image region. This simultaneous readout and exposure of subsequent images facilitates continuous recording of the Earth's surface without data gaps.

At the bottom of the CCD the readout register (ROR) is located. This register is connected to the CCD readout electronics. After being transferred from the storage region the pixels in the readout register are clocked toward the readout electronics and read out. Multiple rows can be collected together (binned) in the readout register prior to the actual readout. This reduces readout time and data rate at the expense of spatial resolution. In the global mode a binning factor of eight is employed, in the spectral zoom-in and in the spatial zoom-in modes the binning factor is four and in unbinned mode the individual rows are read out.

Both regions of the CCD have 576 rows of 780 pixels, each pixel measuring $22.5 \times 22.5\ \mu\text{m}^2$. There is no insensitive area between the pixels. The read out register extends beyond the CCD edges with 17 excess pixels on both sides, which are read out together with every CCD row and serve to estimate dark current and offset.

The CCD pixel full well is $6 \cdot 10^5$ electrons, but above $5 \cdot 10^5$ electrons pixel blooming occurs. In practice the pixel filling is kept below $3 \cdot 10^5$ electrons to prevent the so-called ellipsoid effect, an excessive increase of pixel noise which will be discussed in more detail later. The pixels in the read out register are larger and can hold correspondingly more electrons $(2.5 \cdot 10^6$ electrons) to facilitate binning.

The pixel transfer time is 7.5 μs (133.33 kHz), both for a row (vertical) shift and pixel (horizontal) shift. This yields the total image transfer time of 4.32 ms, while the readout of a complete row takes 6.11 ms. The readout electronics converts the charge collected in a pixel in the readout register into a voltage by use of a capacitor. The analogue CCD signals are amplified by the on-chip amplifier in the DEM before being sampled and digitized by the ELU. The gain factor of this amplifier can be set by the ELU. The overall relative gain of the amplifier can be selected as listed in Table II. Four distinct gain regions can be defined on each CCD, with gain switching taking place at identical columns for every row. When a gain switch occurs the read out process is temporarily stalled to allow the amplifier to settle. During on-ground performance testing of the instrument it was found that after a gain switch an overshoot effect occurs, which

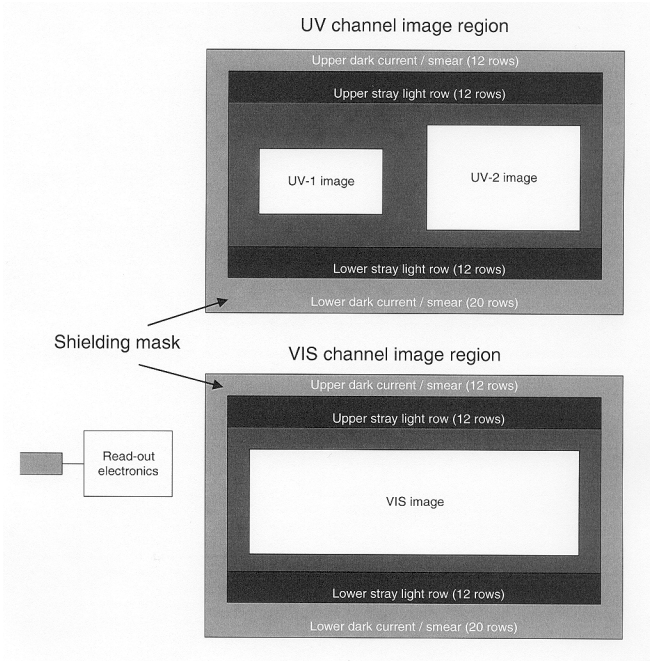

Fig. 11. Schematic layout of the various regions on the OMI CCDs.

shows up as an additional transient on the signal. This overshoot, which originates from a settling effect in the amplifiers, persists for about three columns after the gain switch before disappearing completely. The effect is corrected for in the 0–1 data processing. The amplified analog voltage signal is subsequently sampled and digitized by the ELU using a 12 bits analog-digital converter. The conversion factors are 618.203 and 612.803 electrons per binary unit for the UV and VIS channels, respectively.

Several distinct regions are defined on the CCD detectors. These regions are treated differently in the readout process. The regions, shown in Fig. 11, are the following: Lower dark current and exposure smear region, lower stray light region, image region, upper stray light region and upper dark current and exposure smear region. The spectral image produced by the spectrograph is imaged on the image region, which measures 480 rows in the UV2 and the VIS channel and 240 rows in the UV1 channel. The upper and lower stray light regions are located above and below the image region. They are used to estimate the stray light level in the image. Both regions cover 12 rows and collect the diffuse spectral stray light falling on the CCD outside the illuminated image region. During readout these 12 rows are binned together.

The dark current and exposure smear regions are located at the bottom and top side of the CCD where the pixels are masked. The masked pixels in the dark current and exposure smear regions are insensitive to light and are used to estimate the dark current generation and the exposure smear that occurs when the pixels are transferred through the image, while the illumination of the CCD continues. The lower and upper dark current and exposure smear regions cover 20 and 12 pixels, respectively. Exposure smear is corrected for in the 0–1 data processing.

B. Electronics Unit

The ELU takes care of the complete commanding of the DEM and of the processing of the analog signals originating from the

DEM. Many processes in the ELU, including readout tasks and setting illumination times, are synchronized by the master clock period (MCP). The MCP is the time marker for updating all parameter settings and for producing output. At every MCP the instrument parameters are updated and the digitized CCD images are read out together with the instrument telemetry. In the remainder of this section video data is referred to as science data, whereas parameter settings are named engineering data. The MCP can be set at any value in the range 2.0016–6.405 s with steps of 50.04 ms. The exposure time ranges from 400.32 ms up to the length of the MCP. Both longer and shorter exposure times are also possible. These off-nominal scenarios are discussed separately below.

When the MCP exceeds the exposure time, a common situation in the OMI instrument operation, the individual exposures are co-added and stored in the ELU. In flight the MCP is always equal to an integer number of exposure times, the so-called coadding factor, which typically lies in the range 2 to 10. At the end of the MCP the co-added image is read out. For the so-called small-pixel column the data are available for only one column per detector per exposure time. The number of small-pixel values per co-added image thus equals the coadding factor.

OMI is operated in the pipeline mode. This implies that while the image is read out, the exposure of the subsequent image takes place. The readout time is limited to 400 ms and as a result does not exceed the exposure time. In this limited read out time only 65 rows are read. These 65 rows suffice to fully read a global image: 60 binned image rows correspond to 480 unbinned image rows for binning factor eight, the four stray light and dark current and exposure smear regions are each binned in a separate row, and one row is used to store the readout of the empty readout register.

For lower binning factors the limitations posed by the data rate and the read out time do not allow the entire CCD image to be read out. As a result either rows or columns are skipped in the read out process. In case of spatial zoom-in measurements with binning factor four half of the 480 unbinned CCD rows are read. For spectral zoom-in measurements with binning factor four all unbinned CCD rows are read out in 120 binned rows, but only half of the columns are read out. The result is a 120 rows image with a reduced spectral range.

The binning takes place in the read out register and is realized by clocking in multiple CCD rows and adding the charges before the read out, the number of rows that are binned together in the read out register is called the binning factor. For the purpose of binning the pixels in the readout register are larger in size and can hold up to $2.5 \cdot 10^6$ electrons. Binning the image limits the data size of the output product and improves the signal to noise ratio of the measurement, because the readout noise introduced by the ELU is reduced. The ROR extends beyond both edges of the CCD image and storage sections. These excess pixels, 17 on either side, can be used to investigate the dark current build-up in the ROR. In the read out sequence the lowest storage region row is clocked into the ROR, which is subsequently clocked to the read out electronics pixel by pixel. Before a row is clocked into the ROR its contents are cleared by grounding all pixels in the ROR. This draining of the ROR (drain dump) is required to clear the register from remaining charge of a previous readout or from charge of skipped rows that were dumped in the ROR but not read. In every image that is read out by the ELU the first row is a readout of the dumped ROR. The 17 excess pixels on either side are not cleared in a drain dump.

C. Long and Short Exposure Mode

In the nominal operation of OMI two exposure modes are usually employed: the normal exposure and the long exposure mode. In the normal exposure mode the ELU produces an image after each MCP. When the MCP exceeds the exposure time the individual exposures are coadded and stored in the ELU digital coadder register to be read out after the MCP has been completed.

For measurements that need exposure times longer than the MCP the long exposure mode can be used. This mode is used in flight for dark current calibration measurements. In the long exposure mode an image is not produced after every MCP, unlike in the normal exposure mode. An image is illuminated for a time equivalent to multiple MCPs before it is read out to the ELU. Also for the long mode the MCP can be chosen in the range from 2.0 to 6.4 s in steps of 50 ms. However, the net exposure time can last up to more than 200 MCPs, corresponding to several minutes. In addition, an independent readout of the storage section is available. At the end of the image integration the storage region is read out first, which takes either one or ten MCPs, depending on the binning factor. When the storage region has been read out the image in the image region is transferred to the storage region and subsequently read out. In the same way as for the normal exposure mode the read out of an unbinned image is done in ten steps. After each MCP a data block of 58 rows is read out. The rows that still have to be read out remain in the storage region until the next MCP. In contrast to the normal exposure mode the image does not have to be re-exposed after each partial readout. Consequently, the top of the image resides for a longer time in the storage region and has a correspondingly higher dark current build-up. This effect shows up as a dark current wedge over the image. Another inherent feature of the long exposure mode is that the net exposure time for the storage region is ten MCPs shorter than that of the image region. In contrast to the normal exposure mode the ROR is not cleared prior to the first readout in the long exposure mode (see below), but contains the dark current accumulated during the integration time. This provides information about the dark current build up of the ROR.

Exposure times shorter than the read out time of 400 ms are in principle possible, but such scenarios are not part of the in-flight operational baseline. In case of the alternating mode the short exposure time limits the readout time and as a result less rows will be read out, yielding a smaller image. To prevent this the so-called alternating readout mode is available. In this mode a new exposure is only started after the previous image has been read out completely. This alternating readout mode results in complete images at the expense of data gaps in time in which there is no signal collection while the previously measured image is being read out. In flight this would result in data gaps in the flight direction, and for this reason this mode is not operationally used in orbit.

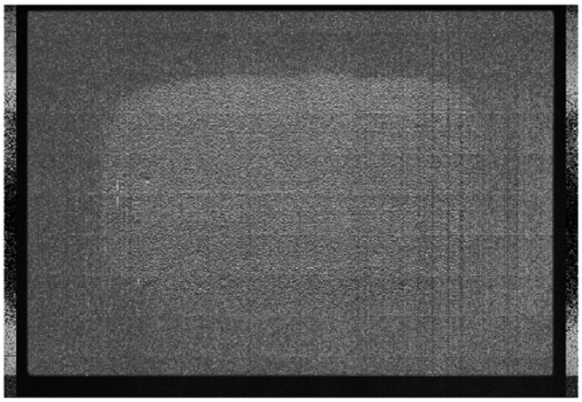

Fig. 12. Ellipsoid effect in the VIS channel. The central ellipsoid-shaped region has increased noise levels.

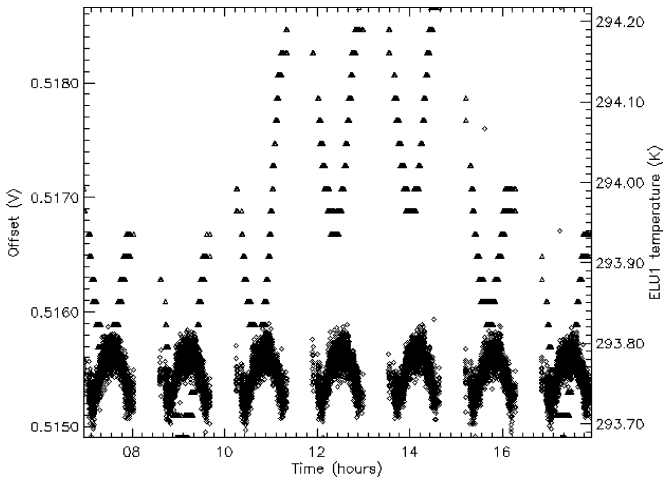

Fig. 13. In-flight electronic offset drifts as a function of time for seven orbits (lower curves, diamonds, left scale). The ELU temperature is shown for reference (top curves, triangles, right scale). These drifts are dynamically corrected by use of the contents of the readout register.

D. Ellipsoid Effect

The capacity of the CCD pixels is $6 \cdot 10^5$ electrons. Beyond this limit the electrons start to spill over the pixel boundaries and leak away to neighboring pixels. This effect, known as blooming, is avoided for nominal operation. At $3 \cdot 10^5$ electrons pixel filling a similar but different effect is observed, the so-called ellipsoid effect. This effect shows up as an ellipsoid shaped band with increased pixel noise on the CCD. In that case the noise increases by one order of magnitude as compared to a pixel filling situation where the ellipsoid effect is avoided. Fig. 12 shows the ellipsoid effect measured in the VIS channel CCD. This effect is caused by random charge diffusion from a pixel to neighboring pixels due to nonuniformities in the voltage barriers. The random nature of the ellipse effect is the reason for its noisy appearance. Again, for nominal operations the exposure times are chosen such that the ellipsoid effect threshold is not exceeded.

E. Offset and Readout Noise

The ELU adds an amplifier gain dependent electronic offset to the measured signals to prevent negative voltages at the ADC input. In case of the highest gain factor this offset amounts to about 1346 BU for the UV channel, about 33% of the 12-bits ADC range. The readout of the empty ROR after a drain dump provides a good measurement for the offset, as the time needed to read the ROR is too short (6 ms) for a significant dark current build up. Fig. 13 shows the in-flight offset drifts in the electronics over seven orbits. The temperature of the electronics is also shown for reference. To compensate for the offset drifts in the image, the 0–1 software uses a dynamically determined offset for correction. The correction values are based on the contents of the ROR. The gain-dependent offset values for UV and VIS are given in Table II.

The noise in OMI measurements consists of shot noise from the signal detected at the CCD (useful signal, stray light and dark current) and readout noise. The readout noise can be derived per pixel from the variance in histograms distributions of time series of dark measurements. The resulting readout noise for each gain setting is given in Table II for both channels.

V. Radiometric Calibration

The radiometric calibration of the OMI instrument can be divided into separate parameters. The absolute radiance and irradiance radiometric calibrations provide the radiometric calibration parameters for the Earth and sun measurements, respectively. As discussed above in the description of the optical design of the OMI instrument, most of the optical components are common to the radiance and irradiance optical paths. The optical sensitivity of these common components thus cancels in the ratio of the Earth and sun measurements, and equally in the ratio of radiance and irradiance calibrations. This ratio is called the OMI instrument bidirectional scattering distribution function (BSDF). This BSDF can be determined with higher accuracy than the absolute radiance and irradiance calibration parameters. The BSDF, i.e., the ratio of the radiance and the irradiance calibrations, is in first order determined by the optical components that are not common to the radiance and irradiance modes. Thus, the BSDF can be approximated by the ratio of the primary telescope mirror 003 in the radiance mode over the solar mesh, the onboard diffuser and the folding mirror C03 in the irradiance mode. Therefore, unlike the radiance and irradiance calibrations, it is a smooth and regular function of wavelength and viewing angle. The BSDF calibration determines the calibration of the in-flight absolute Earth reflectance measurement data. The absolute Earth reflectance data are used as input for nearly all scientific atmospheric retrieval algorithms. This makes the OMI instrument BSDF the most important radiometric calibration parameter. It is discussed first in the sections below.

The irradiance calibration is a function of the incident azimuth and elevation angles on the onboard diffusers. This angular dependence is called the irradiance goniometry. Furthermore, the irradiance calibration is influenced by spectral and spatial features originating from the onboard diffusers, as discussed in Section III-C. The irradiance goniometry calibration and the diffuser spectral and spatial features are discussed separately below.

A. BSDF Calibration

On ground the OMI BSDF has been measured using dedicated optical stimuli. Since the BSDF is a ratio of the radiance and irradiance calibrations, it is not important to use a light source for which the output flux is known accurately in absolute sense. It is sufficient that the light source has a beam divergence that is comparable to the sun (about 0.5°), that the output spectrum is smooth as a function of wavelength in the range 270–500 nm, unpolarized, of sufficient intensity and temporal stability and sufficiently homogeneous spatially and angularly. It is important that the exact same light source is offered to the radiance and irradiance optical ports as close in time as possible. A dedicated optical stimulus fulfilling all these requirements was produced and used during the on-ground calibration campaign. The output beam was about 10 cm in diameter. The used lamp was a 300-W xenon high-pressure arc discharge lamp, which produces sufficient ultraviolet output.

The BSDF is a function of wavelength (CCD column), viewing direction (CCD row) and incident angles of the diffuser. The goniometry is discussed separately below; the results in this section are for the nominal azimuth (25.75°) and elevation (0.0°) angles. The measurements were performed with the instrument in flight-representative thermal-vacuum conditions (pressure $< 10^{-5}$ mbar, temperature optical bench 264 K, temperature CCD detectors 265 K) in a thermal-vacuum chamber with optical windows in front of the Earth and sun ports of the OMI instrument. The optical beam from the stimulus is sufficient to illuminate the complete onboard diffuser, which is about 4 cm in length. This implies that the entrance slit 008 is illuminated completely and that all viewing directions on the CCD detectors are illuminated simultaneously.

This is not the case for the radiance mode. In the radiance mode the exact same stimulus illuminates an accurately calibrated spectralon plate at an angle of incidence of 50.0°. The 10 cm diameter spot on the spectralon plate subsequently illuminates the radiance port of the instrument. The instrument views the spectralon plate at an angle of 40.0°. Care is taken to equal the distances between the optical stimulus and the onboard diffuser in the irradiance mode on one hand and the optical stimulus and the spectralon plate in the radiance mode on the other hand. At a typical distance of 2 m (the exact distance is not crucial for radiance calibration as long as vignetting is excluded) between the instrument and the spectralon plate the illuminated viewing angle is about 3° out of the total OMI viewing field of 115°. This example shows that it is not possible to illuminate the entire 115° field of view of OMI instantaneously. The instrument has to be rotated in about 50 steps and at each step the BSDF for the viewing angle in question has to be calibrated. A complicating factor is that this rotation procedure could not be performed in thermal-vacuum, because the required thermal-vacuum rotational devices were not available. The full range of view angles was measured in radiance mode only under ambient conditions.

In thermal-vacuum conditions the BSDF of the OMI instrument was calibrated for a subset of viewing angles of $-50°$, $0°$, $+50°$. Fig. 14 shows the measured BSDF results for a viewing angle of 0° for the three onboard diffusers. It can be observed that the curves are smooth functions of wavelength,

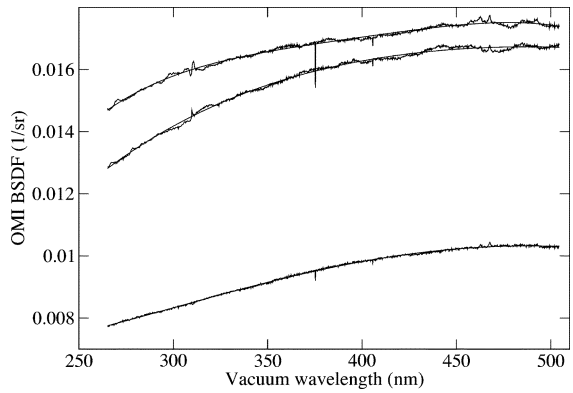

Fig. 14. Measured and fitted OMI instrument BSDF for the three onboard diffusers for nadir viewing angle and nominal azimuth and elevation angles. The curves show the BSDF results for the backup aluminum diffuser, the regular aluminum diffuser, and the quartz volume diffuser from top to bottom.

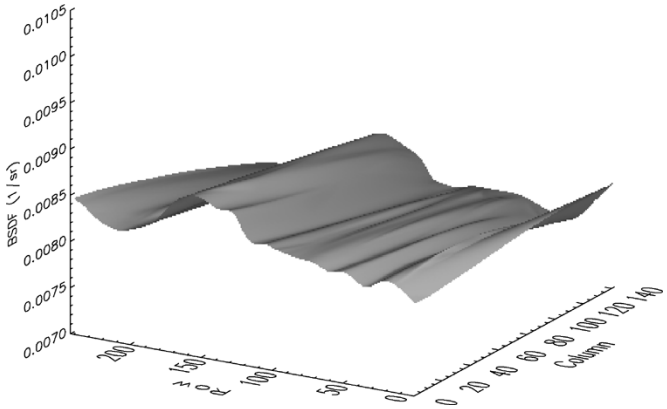

Fig. 15. OMI instrument BSDF for the quartz volume diffuser as a function of column (wavelength) and row (viewing direction) for the UV1 channel for nominal azimuth and elevation angles. The central nadir viewing direction corresponds to row 119. Wavelengths decrease with increasing column number.

apart from some structure resulting from the optical stimulus and the onboard diffuser features. Combination of the ambient and thermal-vacuum measurement sets enabled calibration of the OMI instrument BSDF for all required viewing directions over the complete 115° field of view for flight-representative thermal-vacuum conditions. The result is shown in Figs. 15–17 for the quartz volume diffuser. In these figures different structures as a function of viewing angle can be distinguished. First, in all three optical channels a peak with an amplitude of about 5% in the UV1 and UV2 channels and about 7% in the VIS channel can be observed of about 100 rows wide around the central row nadir viewing direction. This structure is consistently measured in all on-ground measurements, irrespective of the employed external light source. Furthermore, this peak shifts over the rows when the azimuth angle on the onboard diffuser is varied (see also Section V-C). This real structure is tentatively attributed to close-to-specular angle internal reflections between the diffuser surface and the backside of the solar mesh. Second, higher frequency structures over the rows with amplitudes of at most 1% are observed in the BSDF figures. These features are not reproducible for different measurements obtained with different external light sources. They are not part of the real instrument BSDF, but they are an artefact from the way the measurements were performed and analyzed. The

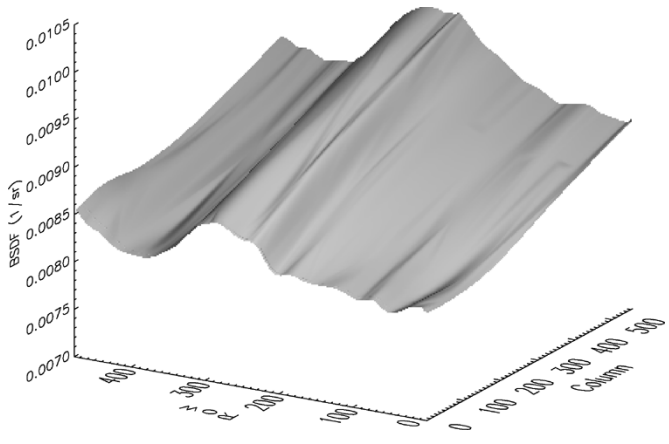

Fig. 16. OMI instrument BSDF for the quartz volume diffuser as a function of column (wavelength) and row (viewing direction) for the UV2 channel for nominal azimuth and elevation angles. The central nadir viewing direction corresponds to row 240. Wavelengths increase with increasing column number.

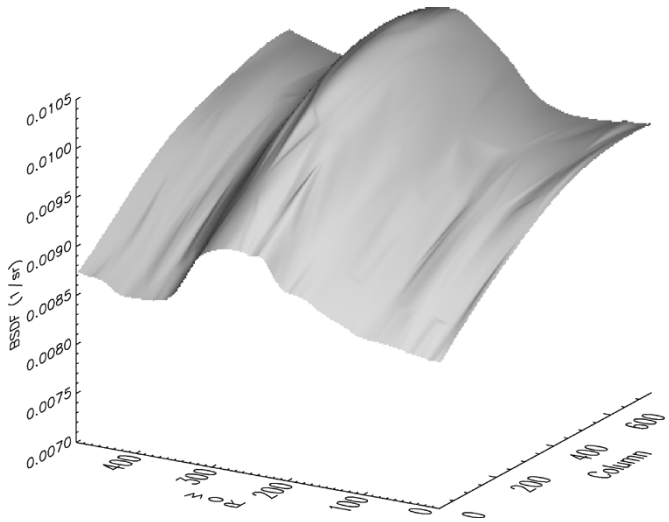

Fig. 17. OMI instrument BSDF for the quartz volume diffuser as a function of column (wavelength) and row (viewing direction) for the VIS channel for nominal azimuth and elevation angles. The central nadir viewing direction corresponds to row 240. Wavelengths increase with increasing column number.

complete 115° field could not be filled instantaneously in the radiance mode, but measurements at different viewing directions had to be performed and put together in the subsequent analysis, which results in the residual higher frequency ripples. These ripples are the main contributor to the swath angle dependency uncertainty of the instrument BSDF as described below.

During the OMI instrument BSDF calibration the unknown BSDF of the instrument is calibrated against the known BRDF of the external spectralon plate, which is close to, but not exactly equal to, $1/\pi$ 1/sr, the expected number for a perfect Lambertian diffuser. The spectralon BRDF is calibrated with an accuracy of about 1% (2σ) [11]. The light flux originating from the spectralon plate is attenuated by the cosine of the incident angle, in this case 50.0°. The final accuracy for the OMI instrument absolute BSDF radiometric calibration parameter as determined on ground using the methods described above is about 4% (2σ). The swath angle dependency of the BSDF is accurate to about 2% (2σ). This uncertainty results from the variations between the various measurements obtained with different external light sources and from the previously discussed higher frequency structures (measurement/analysis artefacts) in the BSDF as observed in Figs. 15–17.

In flight the absolute irradiance calibration can be verified accurately, because the solar irradiance is known to an accuracy of 1% to 2%. This is discussed below. On the other hand, the radiance signals that are measured by the OMI instrument in flight are highly variable as a result of varying ground albedo, varying atmospheric conditions (clouds, composition) and varying illumination conditions. This variability is transferred into the measured in-flight absolute reflectance levels. This makes in-flight validation of the Earth reflectance data, and thus indirectly of the OMI instrument BSDF, difficult and time-consuming. The OMI BSDF will be verified using techniques developed for TOMS and other BUV instruments. Methods typically involve comparisons between observed and theoretical reflectances, and can also include direct comparisons with other satellite measurements. Most comparisons are of total column ozone, with which a radiative transfer forward model can be used to infer the radiometric calibration. However, the measured Earth reflectances (actually the solar-normalized radiances) can be verified directly using stable ground scenes, such as over Antarctic and Greenland ice [12], [13]. Using existing measurements of surface reflectance [14], radiative transfer models are used to predict top-of-the-atmosphere solar-normalized radiances. More work is required in the future to continue and improve such comparisons.

B. Absolute Radiance and Irradiance Calibration

The absolute radiance and irradiance calibrations are important for understanding the radiometric behavior of the instrument on the ground and in flight. This understanding is crucial for proper interpretation of the in-flight optical throughput degradation behavior that will occur at some stage in flight. By comparing the temporal behavior of in-flight measurement results via different optical paths it becomes possible to identify the optical components that are responsible for the observed behavior.

On ground the absolute radiance and irradiance calibration parameters were determined using NIST-calibrated 1000-W FEL quartz tungsten halogen lamps. In total four of these lamps have been used in order to improve the final accuracy. In the irradiance mode the FEL lamps illuminated the onboard diffuser(s) directly via the irradiance port of the thermal-vacuum chamber. The distance between the lamp and the onboard diffuser was 1363 ± 2 mm. The azimuth and elevation angles were nominal. The absolute irradiance calibration measurements are very similar to the BSDF irradiance measurements described above, with the only difference being the light source. In the radiance mode the FEL lamps illuminated the same spectralon plate as used for the BSDF calibration at a distance of exactly 50.0 cm and at normal incidence. The OMI instrument views the spectralon plate at an angle of 40.0°. The distance between the OMI instrument and the spectralon plate was about 2 m. These absolute radiance and irradiance measurements were performed under flight representative pressure and temperature conditions in a thermal-vacuum chamber.

TABLE III
COMBINATION OF AVAILABLE MEASUREMENT DATA TO OBTAIN THE RADIOMETRIC CALIBRATION PARAMETERS. TV INDICATES MEASUREMENTS AT FLIGHT-REPRESENTATIVE THERMAL-VACUUM CONDITIONS

BSDF		Radiance		Irradiance	
nadir	off-nadir	nadir	off-nadir	nadir	off-nadir
Irradiance and Radiance, Xe source (TV)	Radiance, Xe source (ambient) + Irradiance, Xe source (TV)	FEL (TV)	BSDF off-nadir + Irradiance off-nadir	BSDF nadir + Radiance nadir	Xe source (TV)

As with the dedicated BSDF measurements described in Section V-A, only a small range of the 115° field of view could be illuminated instantaneously for the absolute radiance calibration measurements. Multiple radiometric measurements were made during OMI prelaunch testing. These included BSDF radiance and irradiance measurements using an uncalibrated xenon optical stimulus and calibrated FEL lamps for radiance and irradiance sensitivity. All measurements were performed in both ambient and flight-representative (thermal-vacuum chamber) conditions. In the thermal-vacuum chamber absolute radiometric radiance calibration measurements could be obtained only for the nadir viewing direction. While the flight-representative measurements were preferred, the off-nadir radiance measurements were only obtained under ambient conditions. Verification measurements were performed in flight representative conditions for a subset of viewing angles. Also, the signal-to-noise of measurements using the xenon light source was superior in the ultraviolet to those using the FEL. The BSDF derived using the two sources was found to be in agreement within the noise levels, so data from the former were used for BSDF determination whenever possible.

All these measurements were carefully analyzed and combined to obtain the radiometric calibration parameters in the following way. The particular way in which measurements were combined, shown in Table III, was chosen to maximize data from flight-representative conditions, maximize signal-to-noise, and maintain consistency between the various radiometric parameters. The off-nadir calibrations were computed as the product of calibrations at nadir and a set of relative factors that vary with viewing angle. Consequently, the uncalibrated source could be used for off-nadir parameters. The absolute irradiance measurement results have comparatively low signal-to-noise because the solar mesh and the diffuser reduce the light flux from the FEL lamp considerably. For this reason the absolute FEL lamp radiance calibration results were combined with the BSDF results from the other optical stimulus to obtain the absolute irradiance calibration, which is in turn in agreement (within the noise levels) with the absolute irradiance measurement itself.

The resulting absolute radiance results (in photons per square centimeter per nanometer per steradian per electron) and irradiance results (in photons per square centimeter per nanometer per electron) for the three onboard diffusers are shown in Fig. 18.

Fig. 19 shows the solar irradiance spectrum measured in flight with the quartz volume diffuser and binning factor eight for row 33 on February 20, 2005. This spectrum can be compared

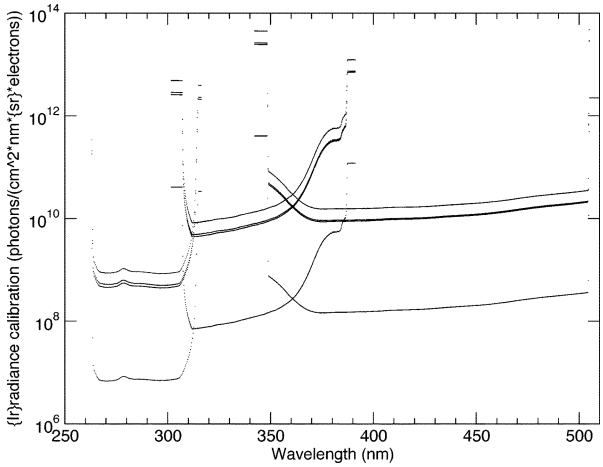

Fig. 18. Absolute radiance (bottom curve) and irradiance (top three curves) calibration data for the nadir viewing direction. These data produce the smooth OMI instrument BSDF results as shown in Fig. 15. The top curve is for the quartz volume diffuser, and the other two irradiance curves are for the aluminum diffusers.

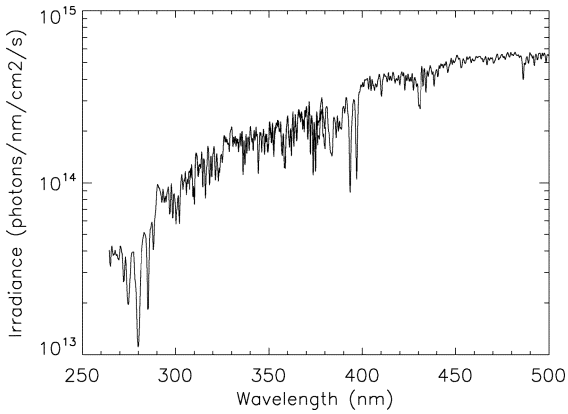

Fig. 19. Measured solar spectrum over the quartz volume diffuser with binning factor eight for row 33 (orbit 3207, February 20, 2005).

to the literature high-resolution solar spectrum convolved with the OMI spectral slit function. The OMI spectral slit function was measured very accurately on the ground using a dedicated measurement setup and analysis method (Section IX). The convolved spectrum is not shown in Fig. 19, because it nearly coincides with the measured spectrum. The ratio of the two spectra is shown in Fig. 20. From this ratio a couple of observations can be made.

First, there is a more or less wavelength dependent offset of about 3% to 4%, which can be traced back to a multitude of particular artifacts in the measurement setup and methods used during the on-ground calibration, e.g., stray light in the thermal-vacuum measurement setup, accuracy of spectralon reference plate calibration, lamp irradiance calibration, etc. Second, the residual Fraunhofer structures are comparatively small, although the results can certainly be optimized further in this respect. The figure shows that the convolution of the high-resolution literature solar spectrum with the measured spectral slit functions reproduces the measured solar Fraunhofer structures reasonably well, which suggests that both the literature solar spectrum and the slit functions are quite accurate. It further shows that the wavelength calibration attached

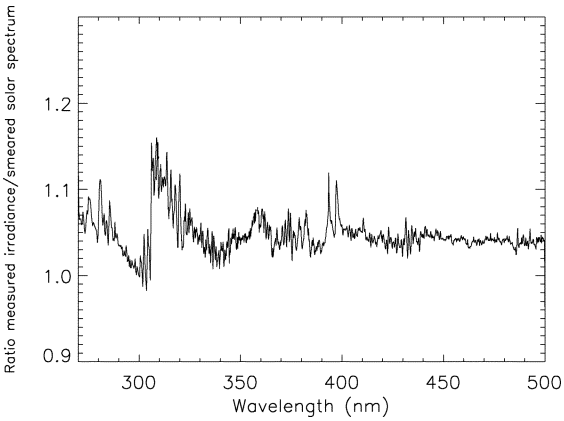

Fig. 20. Ratio of solar irradiance measurement over the quartz volume diffuser with binning factor eight (orbit 3207, February 20, 2005) and the high-resolution solar reference spectrum convolved with the measured OMI spectral slit function.

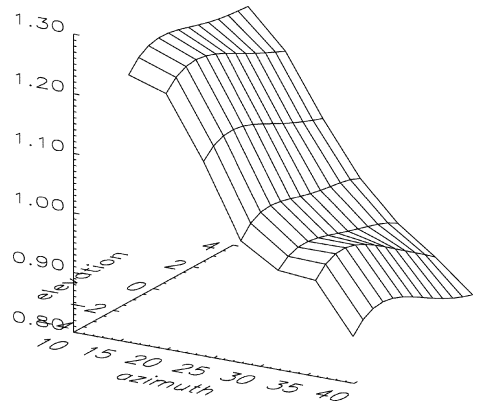

Fig. 21. Irradiance azimuth and elevation angle (in degrees) dependence for the quartz volume diffuser for unbinned row 100.

to the measured solar spectrum is accurate to typically a few hundredths of a pixel. The OMI wavelength calibration is based on the measured solar spectrum, so the algorithm is working well. Further optimization in the mentioned areas is of course planned. Third, differences are observed in the channel overlap regions, especially between UV1 and UV2 at about 305 nm. This suggests that the wavelength dependence of the absolute radiance and irradiance calibration needs to be revisited and optimized. This needs to be done in a way that no wavelength dependent structure is introduced in the ratio of the two, i.e., the instrument BSDF. Despite the need for further improvement, the accuracy of the results shown in Figs. 19 and 20 is not unexpected, given the complexity of the OMI design and calibration. Once the accuracy of the irradiance goniometry calibration (see Section V-C) has been improved using in-flight measurement data we will start investigating in detail the in-flight degradation behavior of the onboard diffusers. Preliminary results show that the diffusers have not degraded more than about 0.5% for all wavelengths in the OMI wavelength range 264–504 nm.

C. Irradiance Goniometry

In addition to depending on wavelength (column) and viewing direction (row), the irradiance calibration depends on the incident angles on the onboard diffusers. As outlined in Section III these comprise the elevation angle, which varies from $+4.0^\circ$ to -4.0° around the nominal value of 0.0°, and the azimuth angle, which varies slowly throughout the year from about 21° to 31° around the nominal value of 26.0°. As explained in Section III the real elevation angle on the diffuser varies around 11°. The elevation angle change originates from the satellite orbital movement during a solar observation sequence of 154 s. The elevation angle change during each of the 77 images is about 0.1°. Each individual image needs to be corrected for the radiometric goniometry. The irradiance goniometry correction factors are multiplicative factors, which are by definition 1.00 for the nominal azimuth and elevation angles. Once this has been done, the images in the elevation angle range $[-3.0^\circ; +3.0^\circ]$ obtained during one solar observation sequence are averaged to improve the signal-to-noise. The radiometric irradiance calibration is thus a complex function of wavelength, viewing angle, elevation angle and azimuth angle for each of the three onboard diffusers.

The irradiance goniometry was calibrated on ground. The same optical stimulus as used for the BSDF measurements (see Section V-A) was also used for these measurements. The instrument needs to be rotated about two axes that are located on the diffuser surface to cover the elevation and azimuth angle ranges. Since this could not be done in the thermal-vacuum chamber the measurements were necessarily performed under stabile ambient conditions (293 K). The actual irradiance goniometry is not expected to change from air to vacuum or with temperature, because this concerns the optical properties of the diffusers, for which no optical mechanisms are known to cause such changes. However, the performance of the CCD detectors is considerably worse at 293 K than at 265 K, the operational temperature. This leads to a set of irradiance goniometry measurement data with low signal-to-noise. Only a limited subset of azimuth and elevation angles could be measured for the three diffusers on the ground. The remainder of the data cube was obtained by interpolation (in two dimensions) between the available angles, which introduces additional uncertainties. Furthermore, the illumination geometry is close to, but not completely identical to, the illumination geometry in flight. This too introduces additional uncertainty. Despite the limitations of the available on-ground measurement dataset, an analytical functional dependence on row, elevation, and azimuth angle was found and calibration data for this function were derived. It was found that there is virtually no dependence on wavelength. It was not possible to factorize the other variables into separate functions. These data are used in the 0–1 data processor to correct for the irradiance goniometry. Figs. 21–24 show a number of examples for some rows for the quartz volume and regular aluminum onboard diffusers. The magnitude of the goniometry correction is usually between 0.8 and 1.2, but can be as large as 1.3 for extreme angles. The accuracy of the reconstructed goniometry data as compared to the measured data was found to be about 2%.

The accuracy of the irradiance goniometry correction can be determined in flight. Furthermore, given the accuracy of the available on-ground irradiance goniometry measurement data, it will be necessary to derive new calibration data based on the in-flight irradiance data at various elevation and azimuth angles. In order to do this properly the full azimuth range will need to be covered, which will take one year. Preliminary studies on

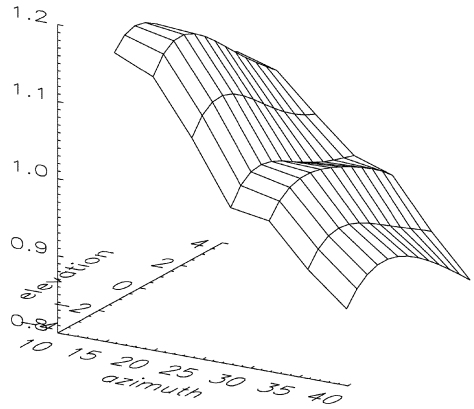

Fig. 22. Irradiance azimuth and elevation angle (in degrees) dependence for the quartz volume diffuser for unbinned row 500.

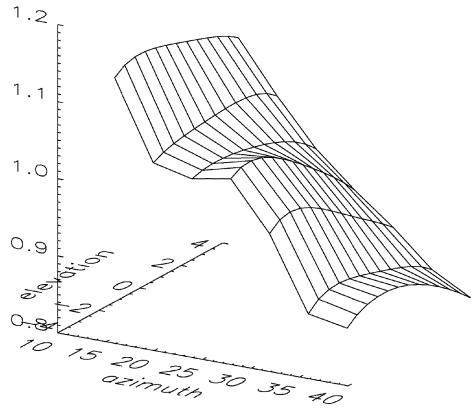

Fig. 23. Irradiance azimuth and elevation angle (in degrees) dependence for the quartz volume diffuser for unbinned row 288 (nadir view).

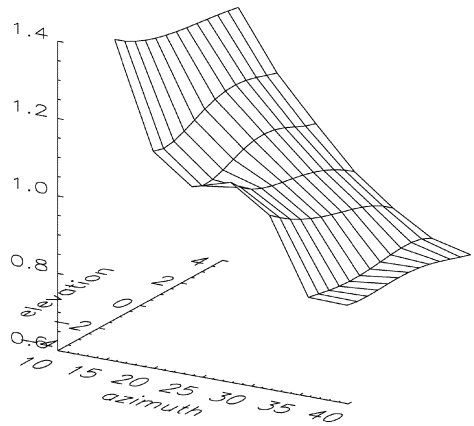

Fig. 24. Irradiance azimuth and elevation angle (in degrees) dependence for the regular aluminum diffuser for unbinned row 288 (nadir view).

the validity and accuracy of the available goniometry irradiance correction data indicate that the accuracy of the irradiance goniometry calibration is about 3%, more or less in line with the expectations from the on-ground calibration data. It is expected that accuracy of the irradiance goniometry calibration can be increased to better than 0.5% by using the available in-flight measurement data.

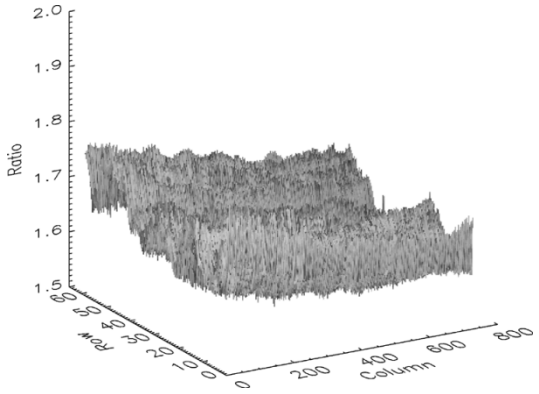

Fig. 25. Ratio of regular aluminum and quartz volume diffuser L0 irradiance data of December 30, 2004 (elevation angle 0.0°, azimuth angle 25.8°) for the visible channel. The figure shows the diffuser features of the regular aluminum diffuser as a function of viewing direction and wavelength.

D. Diffuser Spectral and Spatial Features

As explained in Section III-C the OMI instrument response is affected by the surface structure of the three onboard diffusers, because each pixel only views a few square millimeters of diffuser surface. This behavior is already known from other satellite instruments such as GOME on ERS-2 and SCIAMACHY on ENVISAT, which use reflective aluminum diffusers in a manner optically similar to that of OMI. Initial measurements with OMI showed that the aluminum diffusers introduce spectral and spatial features on the CCD images of the irradiance mode with peak-peak amplitudes of 5% to 10% for unbinned images. From an optical performance point of view, this was deemed too much for DOAS applications, where residual structure in the Earth reflectance data is detrimental for the accuracy of the gas retrievals. The appearance of the spectral and spatial features as a function of row or viewing direction and column or wavelength changes drastically with incidence angle on the diffuser, both with azimuth angle and elevation angle. This makes it virtually impossible to correct for the features or calibrate them out. For these reasons a dedicated diffuser with optimized spectral and spatial feature behavior was developed for the OMI instrument. This is the quartz volume diffuser, for which the optical and operational details were given in Section III-C.

To understand the appearance of the diffuser features we refer to the following figures. Fig. 25 shows the in-flight ratio of the regular aluminum diffuser over the quartz volume diffuser in the visible channel. The features are much smaller in amplitude for the quartz volume diffuser than for the aluminum diffuser (see below), so the figure essentially shows the spectral and spatial features of the aluminum diffuser. It can also be observed that the regular aluminum diffuser has a 1.7 higher efficiency than the volume diffuser at this wavelength range (350–500 nm). The structures, with peak-to-peak amplitudes of about 10%, are mainly wavelength independent (changes with row or viewing direction and not with column or wavelength), but there are also spectral features within each row. The result shown in Fig. 25 is for binning factor eight. Binning has been observed to reduce the spectral features efficiently and the spatial features to some extent. Fig. 26 shows the ratio of individual elevation angles over the average of all elevation angles for both types of diffuser as

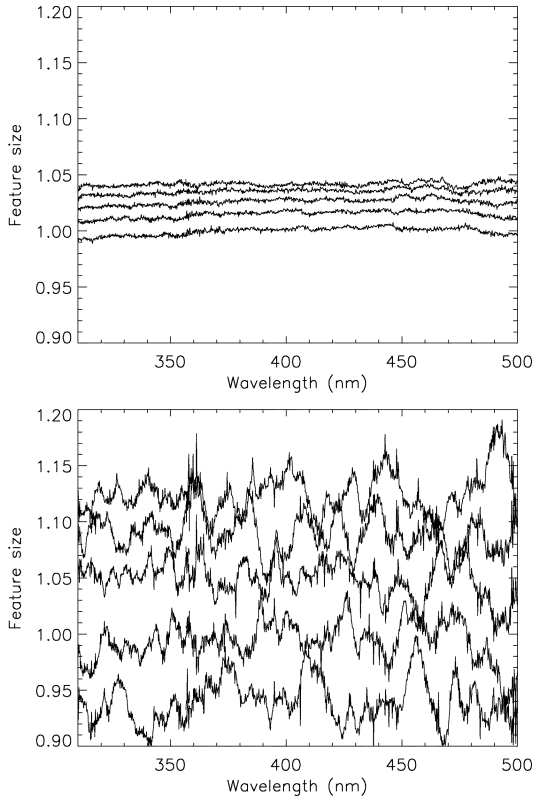

Fig. 26. Ratio of single elevation measurement over the average of all elevation angles in the range $[-3.0°, +3.0°]$ for (top) quartz volume diffuser and (bottom) aluminum diffuser in the wavelength range 310–500 nm as measured on the ground. The elevation angles run from $-1.0°$ at the top to $+1.0°$ on the bottom in steps of 0.5° in both figures.

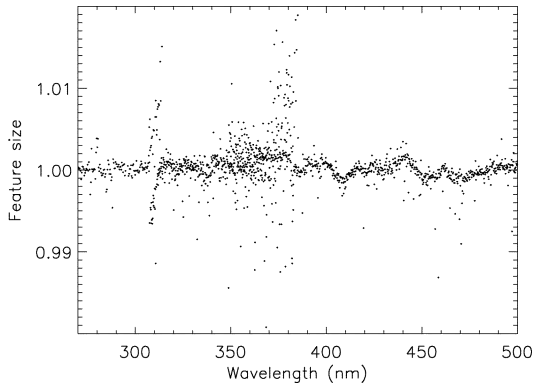

Fig. 27. Ratio of L1 irradiance data with azimuth angle 30.0° (November 18, 2004) divided by azimuth angle 26.9° (December 20, 2004) via the quartz volume diffuser, showing the achieved in-flight diffuser features after binning eight rows and averaging over the elevation angle range.

measured on ground. Already from these on-ground measurements the superior feature behavior of the quartz volume diffuser over the aluminum diffuser is apparent. This observation is confirmed in flight.

The origin of the features is twofold. First, the instrument views the surface structure of the diffusers over a few millimeters, because the diffusers are located close to the focus of the telescope system. The diffuser loses its randomizing behavior at this scale, and reflectance becomes nearly specular. This causes the nearly wavelength-independent spatial features. Second, decreased randomization of the reflected sun light increases the

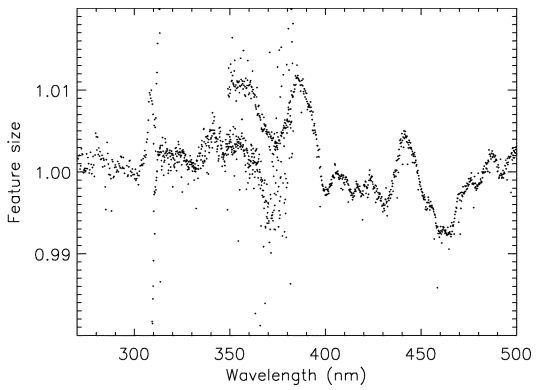

Fig. 28. Ratio of L1 irradiance data with azimuth angle 30.0° (November 18, 2004) divided by azimuth angle 26.9° (December 20, 2004) via the regular aluminum diffuser, showing the achieved in-flight diffuser features after binning eight rows and averaging over the elevation angle range.

degree to which interference occurs, resulting in spectral features with periods of 20–30 nm in the visible wavelength range (e.g., Fig. 27). These features are expected to become smaller in amplitude and shorter in period toward the ultraviolet. This has indeed been observed in measurements on component level. Given the variability of the features with illumination geometry it is virtually impossible to calibrate them out, but there are two ways of reducing their impact. Both ways utilize the fact that the features vary with viewing direction and elevation angle. In normal global operation of the instrument, electronic on-chip binning takes place (see Section IV-A). The signals of eight rows are coadded. This improves the signal-to-noise and reduces the data rate, but it also reduces the impact of the diffuser features roughly by a factor sqrt(8). Second, the solar images obtained at different elevation angles in the range $[-3.0°; +3.0°]$ are averaged after radiometric correction. This also improves the signal to noise roughly by a factor 8 and reduces the amplitudes of the features by the same factor. Both effects combined result in a reduction of the features by a factor of about 20. Figs. 27 and 28 show the remaining spectral features after binning and averaging over the elevation angle range for the quartz volume diffuser and the regular aluminum diffuser. The resulting peak-peak amplitudes are about 0.3% for the quartz volume diffuser and 1.8% for the regular aluminum diffuser for the central row, which is shown in these figures. The figures show the ratios of two azimuth angles at 30.0° and 26.9°, so the peak-peak amplitudes in the individual measurements will be about half of those numbers, i.e., about 0.15% for the quartz volume diffuser and 0.9% for the regular aluminum diffuser.

Another interesting feature can be observed when the azimuth dependence is investigated. Fig. 29 shows the ratio of two uncalibrated irradiance measurements obtained at two azimuth angles (25.8° and 30.0°) on different dates (December 30 and October 17, 2004, respectively) for the visible channel of the quartz volume diffuser. This ratio shows an attenuation of about 12% as a function of viewing direction. This effect is tentatively attributed to interference effects in the cavity between the solar mesh and the onboard diffuser, which has a width of about 10 mm. Back reflections from the diffuser hit the mesh and reilluminate the diffuser. This effect, which has been observed both on the ground and in flight, is calibrated out in the irradiance goniometry calibration. From Fig. 25, where the attenuation is

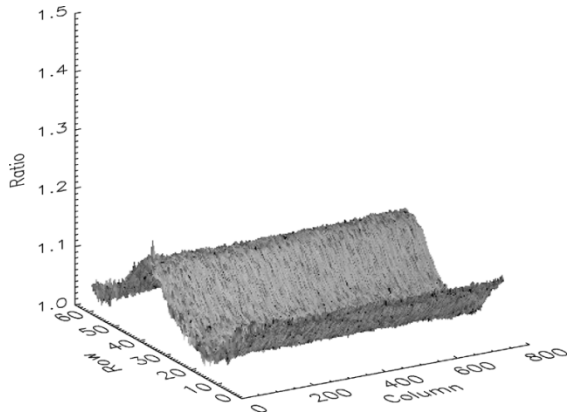

Fig. 29. Ratio of quartz volume diffuser L0 irradiance data of October 17, 2004 (elevation angle 0.0°, azimuth angle 30.0°) and December 30, 2004 (elevation angle 0.0°, azimuth angle 25.8°) for the visible channel. This ratio of two azimuth angles shows, besides minimal diffuser features, also a radiometric attenuation originating from interference between the solar diffuser and the solar mesh.

absent in the ratio of two diffusers, and from other observations it can be seen that this wave-like attenuation is the same for all three onboard diffusers.

E. Optical Throughput Degradation of the Instrument in Flight

The optical throughput of the instrument can be monitored in flight in a relative sense, i.e., as a function of time with respect to the beginning of the mission. This can be done for various instrument modes. Instrument radiometric monitoring of the radiance port, including the first telescope mirror 003, is difficult due to the variability in the Earth radiance fluxes. This was discussed in Section V-A. The sun also provides a stable and known irradiance source for monitoring the instrument radiometric stability, provided the irradiance goniometry and, in the case of OMI, the onboard diffuser features are well understood. This section will focus on radiometric monitoring of the OMI instrument using the internal white light source (WLS). The prime purpose of the WLS is to provide measurement data to calibrate CCD detector features such as pixel-to-pixel response nonuniformity (see Section XI) and dead and bad pixels. However, the WLS is radiometrically stable to an accuracy of about 0.5% to 1.0% and can be used to monitor the radiometric stability of the OMI instrument in flight. The optical path is more or less the same as for the sun measurements, except for the onboard reflectance diffusers in the sun mode, which are replaced by the transmission diffuser in the WLS mode. In case the WLS response as a function of time is measured to be stable it can be concluded that both the radiometric throughput of the WLS optical path and the lamp itself are stable. In case degradation is observed both the optical path and the lamp can be subject to degradation, and one will have to resort to other modes (sun, Earth) in order to identify the component(s) that cause the observed degradation.

The in-flight optical stability has been monitored using the WLS since launch plus 36 days, when the WLS was switched on for the first time at an instrument temperature of 264 K. Since the WLS illuminates the complete entrance slit and the complete CCD detectors, all pertinent wavelengths and viewing directions can be investigated. Fig. 30 shows the OMI in-flight optical stability from launch plus 36 days until launch plus 200 days for

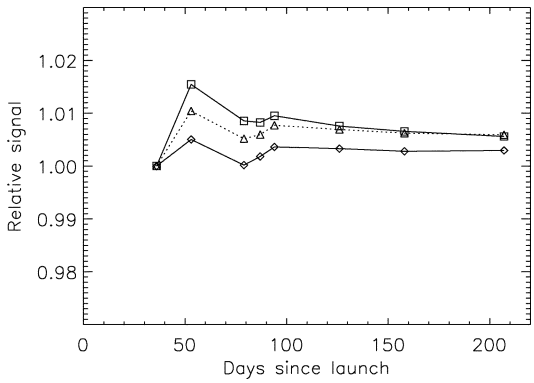

Fig. 30. Instrument optical stability as measured with the internal white light source from launch plus 36 days until launch plus 207 days for UV1 (top line), UV2 (middle line), and VIS (bottom line).

UV1, UV2, and VIS as measured with the WLS. In the figure the averaged response of the complete illuminated area per subchannel is shown, but this result is representative for smaller areas on the CCD as well. It can be seen that in the beginning of the mission there are some settling effects of about 1% to 2%, tentatively attributed to the lamp itself. It can be concluded that no optical throughput degradation can be observed outside the accuracy of the WLS measurements (0.5% to 1.0%) in the time period under investigation. This implies that both the WLS optical path and the lamp itself are stable for this time period.

VI. Viewing Properties

The viewing properties of the OMI instrument determine the geolocations and reflection angles of the observed scenes. They comprise the instantaneous pixel line of sight (PLOS), which is determined by the azimuth and elevation angles of the radiance mode, and the instantaneous pixel field of view (PFOV). Both parameters are functions of column (wavelength) and row (viewing direction) on the CCD detectors. For the line of sight the azimuth angle basically equals the viewing swath angle, which is the range $[-57.5°; +57.5°]$. The elevation angles correct for the smile effect in line of sight, as explained earlier in Section III-A. Finally, the viewing properties comprise the spatial response function, i.e., the viewing direction equivalent of the spectral slit function in the wavelength dimension. If a parallel beam of white light is offered to the instrument via the radiance port, the response on the CCD detectors has a certain shape and resolution. This is the spatial response function. Information on the co-alignment of the three subchannels is also contained in the measurements.

The viewing properties were calibrated on the ground using a parallel white light beam to the instrument via the radiance port. By rotating the instrument using a turn-tilt cradle and monitoring the response per CCD pixel, the viewing properties were calibrated. Alternatively, in some cases the viewing properties are determined by offering a fixed combination of azimuth and elevation angles and examining the response of multiple pixels in the row (viewing direction) dimension. The output beam of the optical stimulus is highly collimated with a divergence about 0.03°, i.e., about 0.1 pixel. The turn-tilt cradle is not suitable for thermal-vacuum environment and for this reason the viewing property measurements were performed

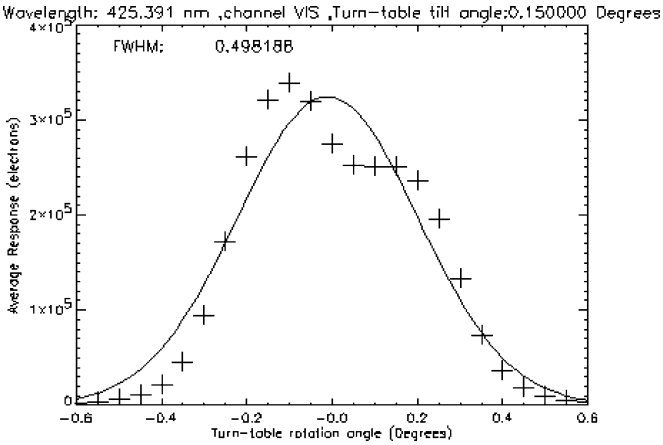

Fig. 31. Measured spatial resolution in the swath dimension for a pixel close to nadir in the VIS channel at about 425 nm along with the fitted Gaussian result. The double peak is originating from the polarization scrambler.

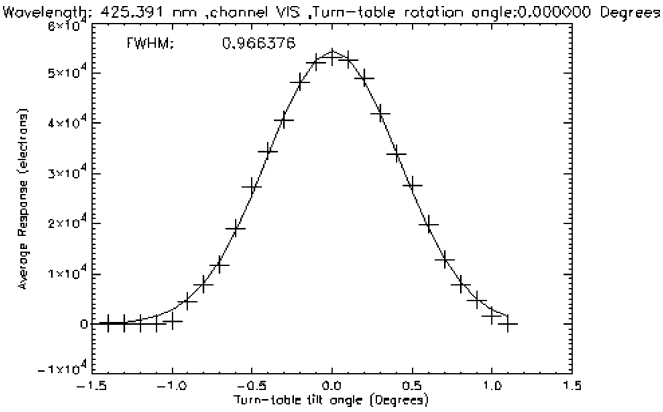

Fig. 32. Measured spatial resolution in the flight direction for a pixel close to nadir in the VIS channel at about 425 nm along with the fitted Gaussian result.

under ambient conditions. A number of measurements were performed to quantify the changes in viewing properties from air to vacuum and from room temperature to the operational temperature of 264 K. The results were included in the viewing property calibration parameters.

The azimuth angle is a nearly linear function of the row numbers. An example of the elevation angle was shown earlier in Fig. 9. The 0–1 data processor averages the azimuth and elevation angles per optical subchannel over all wavelengths in the illuminated image area. The final geolocation per subchannel is calculated using these averaged azimuth and elevation angles.

If the spatial response function in the swath direction is fitted using a Gaussian response the full width at half maximum (spatial resolution) is typically about 2.3 row pixels in UV2 and VIS and 1.6 pixels in UV1. At the extreme viewing angles the spatial resolution is larger: about 3.0 pixels in UV2 and VIS and 2.5 pixels in UV1 at a swath angle of $+56^{\circ}$. If a scan at high resolution is performed it can be observed that the spatial response function in the swath dimension is doubly peaked. As explained in Section III-B, this is caused by the polarization scrambler. An example of this behavior in the VIS channel for a pixel close to the nadir viewing direction is shown in Fig. 31. Fig. 32 shows a similar scan in the VIS channel for the same pixel close to the nadir viewing direction, but in this case in the flight direction. The response function in the flight-direction can be fitted well with a Gaussian shape. The full width at half maximum of about 1.0° and the shape is in good agreement with the measurements on the telescope on component level (see Section III-A).

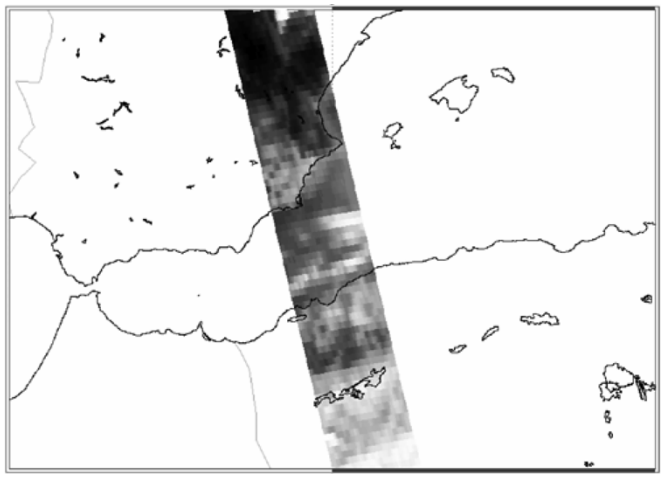

Fig. 33. Typical result using the unbinned superzoom mode central part of the visible CCD over southern Spain and North Africa on November 19, 2004 (orbit number 1853).

The L1 geolocation has been validated in flight. The instrument was operated in a special unbinned mode for several days, providing cross-track resolution at nadir approximately five times that in the normal binned mode. Fig. 33 shows a typical false-color image based on these measurement data in the visible channel plotted on calibrated geolocation latitude and longitude from the L1 radiance product along with the coast contours. From these investigations it can be concluded that the geolocation in flight at various viewing directions on the CCD detectors is accurate to about 0.1 pixel, corresponding roughly to 2 km.

VII. Stray Light

A. Spectral Stray Light

The spectral stray light behavior of the instrument was extensively characterized and calibrated on the ground. The most critical wavelength range, as far as spectral stray light is concerned, is the UV1 channel with wavelength range 264–311 nm, and especially the wavelength range below 290 nm, where the useful radiance signal is two orders of magnitude lower than at 310 nm as a result of the ozone absorption. The optical design of the instrument has been optimized to reduce spectral stray light below 290 nm, as explained in Section III. The uncorrected measured spectral stray light fraction at 270 nm is about 8% of the useful signal. Therefore, an additional correction to reduce spectral stray light below 1% after correction is required.

On the ground spectral stray light measurements have been performed via the radiance port for various viewing directions at ambient conditions. Measurements via the calibration port (see Section III) at both ambient and flight-representative pressure and temperature conditions have also been performed. The employed light source was a high-flux optical stimulus (150-W xenon lamp) with a divergence of about 3° and an output beam of about 5 cm in diameter. Various well-calibrated bandpass and cut-on long-pass wavelength edge filters were used to vary the source area illumination.

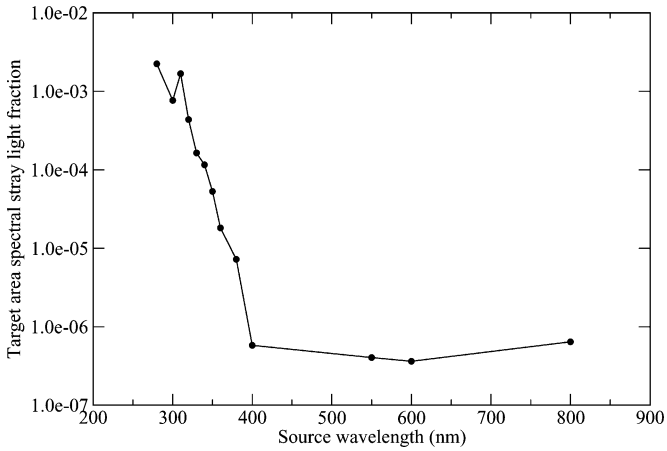

Fig. 34. Spectral stray light fraction in UV1 at 290 nm as a function of the source region wavelength. It can be observed that the largest fractions are from the upper wavelengths in UV1 and the lower wavelengths in UV2.

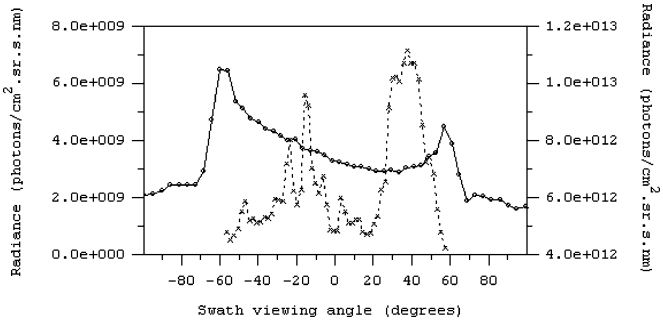

Fig. 35. Radiance distribution as a function of the swath viewing angle for a wavelength where clouds are visible (crosses and dotted line, 313 nm, right vertical scale) and where clouds are not visible (circles and solid line, 280 nm, left vertical scale).

Most of the UV1 stray light (e.g., in the range 265–280 nm) results from near-band scatter (280–350 nm). As a representative example Fig. 34 shows the spectral stray light fraction at 290 nm in UV1 as a function of the source region wavelength. The figure shows that source regions above 350 nm hardly contribute to the spectral stray light in UV1. From all measurements or source regions the spectral stray light in UV1 is fitted with polynomials through the columns (wavelengths), but independently of the rows, in the target area in UV1. A spectral stray light correction algorithm has been implemented in the 0–1 data processing. In that algorithm the source area is radiometrically calibrated and summed over the applicable columns and rows. Validation using the available spectral stray light measurements and zenith sky measurements show that the spectral stray light is reduced by a factor 5–10 using the above algorithm.

The on-ground spectral stray light measurements suffer from low signal-to-noise because of the tradeoff between limiting the spectral source region and having high signal levels. Based upon the ground tests stray light rejection in the UV1 channel appears to be very good. Because the ozone profiling algorithms that use the UV1 signals are sensitive to stray light it is important to validate and possibly optimize the spectral stray light algorithm and calibration parameters using in-flight radiance measurement data. This is an ongoing activity. Some preliminary results are shown in Fig. 35. The figure shows the radiance distribution as a function of the swath viewing angle for a wavelength where clouds are visible (313 nm) and where clouds are not visible (280 nm). The figure shows that the cloud structure does not appear at 280 nm, indicating that the assumption in the stray light correction algorithm to allow source region swath averaging, is justified, and that there is a gradient in the swath illumination for 280 nm which implies that the assumption in stray light correction algorithm to have no swath dependency in the target regions, is not fully justified. More work is required to improve the spectral stray light calibration using in-flight radiance data.

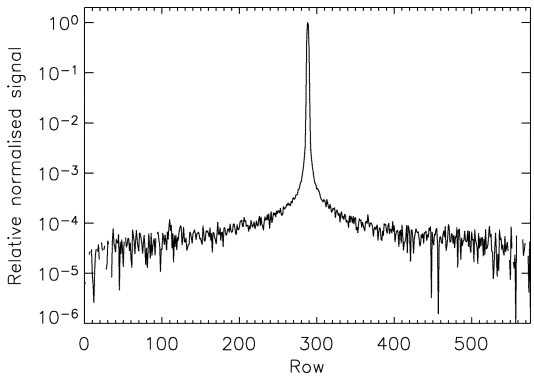

Fig. 36. Spatial stray light at column 300 (about 340 nm) in UV2 with source illumination at nadir. The observed spatial stray levels are as expected from component measurements on the bare OMI telescope.

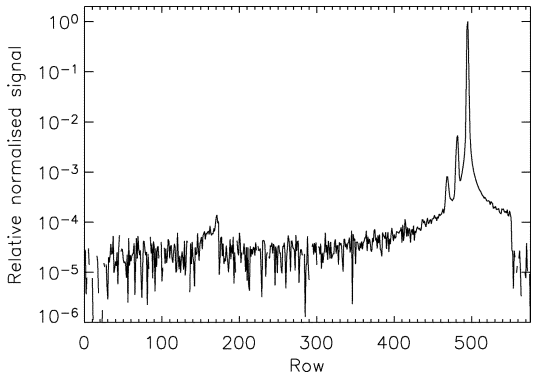

Fig. 37. Spatial stray light at column 400 (about 430 nm) in VIS with source illumination at $-50°$, showing increased stray light at more negative swath angles. In addition, three spatial ghosts can be seen.

B. Spatial Stray Light

Spatial stray light is light intended for a specific viewing direction ending up at another viewing direction. In general, spatial stray light and spectral stray light are mixed, i.e., light can end up at another viewing direction as well as at another wavelength. In this section we discuss purely spatial stray light.

The OMI instrument radiance port spatial stray light behavior has been characterized on the ground. Typically, light is offered to a restricted area of viewing directions covering about 2° to 3°. White light is used, but also some measurements using bandpass filters and cut-on filters, as discussed in the spectral stray light section, have been performed. For measurements under flight-representative thermal-vacuum conditions, only a restricted set of angles could be covered in the available time: swath angles of $-50°$, $0°$, $+50°$. Fig. 36 shows the result for UV2 for nadir. This result is typical for the spatial stray light performance of the telescope as measured on component level, implying that the rest of the optics are not introducing additional spatial stray light

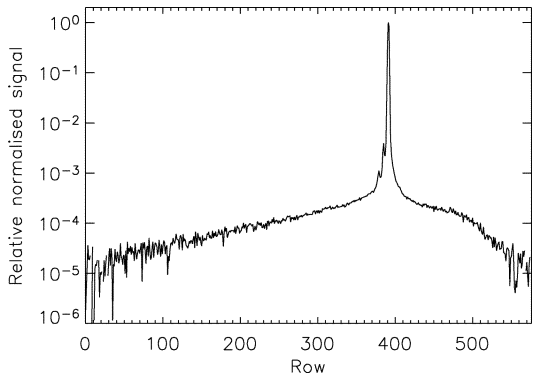

Fig. 38. Spatial stray light at column 700 (about 285 nm) in UV1 with source illumination at $-50°$, showing increased stray light at all viewing directions. In addition, two near-field spatial ghosts can be seen.

effects. No spatial ghosts are observed. Fig. 37 shows a representative result at source illumination $-50°$ for the VIS channel. It can be observed that toward more negative swath angles the background signal is about ten times higher than toward nadir as a result of spatial stray light. In addition two near-field ghosts and one small ghost at a positive viewing angle are observed. Fig. 38 shows a similar result for UV1. It can be observed that additional spatial stray light is measured.

The on-ground measurements present a situation where about 50 rows are illuminated and smeared over 420 other rows, whereas in flight 420 rows can be illuminated and scattered into 50 low-albedo scene rows for certain worst-case high contrast scenes. This makes a difference of typically two orders of magnitude with respect to the situation as shown in Figs. 36–38. In such worst-case situations spatial stray light contributions of one to a few percent could be possible. On the other hand, such worst-case situations are not likely to occur for purely spatial stray light in UV1, because for the wavelength range 260–305 nm the ground and clouds are not visible and high-contrast scenes do not occur for this channel.

No correction algorithm has been implemented in the 0–1 processing for spatial stray light. In future, a correction could be based on a matrix/vector approach, where source region illumination is scattered into different viewing directions based on a wavelength-dependent calibrated spatial stray light matrix. There are no indications in the ground measurements for strong spectral spatial stray light components, so the spatial stray light will be considered as purely spatial. Given the availability of only three viewing angles for the source regions from the on-ground measurements, it will be difficult to fill and verify such a matrix.

VIII. Wavelength Calibration

The in-flight wavelength calibration for OMI is performed by use of the Fraunhofer lines in the sun spectra and Earth spectra. Instruments comparable to OMI often have onboard PtCrNe(Ar) hollow-cathode spectral calibration sources. However, the wavelength calibrations from such sources are of insufficient accuracy for the application of L1 measurement data in DOAS retrievals for a variety of reasons. First, the availability of the spectral lines, their distribution over the instrumental wavelength range and the line blending are often not optimally suited for achieving a very accurate spectral calibration. Second, the optical path from the lamp to the spectrometer is not identical to the optical path that is followed with sun or Earth illumination, or the entrance slit illumination with the lamp is different in terms of uniformity as compared to sun or Earth illumination, which introduces small systematic shifts of the spectral lines on the detectors. More accurate spectral calibrations are derived from Earth and sun measurement data, which is the approach chosen for the OMI instrument in flight. Spectral lamp measurements have been performed on the ground to support the prelaunch wavelength calibration.

During the on-ground calibration spectral calibration data have been obtained by illumination of the calibration port (see Section III) with a dedicated optical stimulus equipped with a PtCrNeAr hollow-cathode spectral light source. Illumination via the calibration port ensures homogeneous filling of the entrance slit and thus instantaneous complete illumination of all viewing directions on the CCD detectors. It was verified that the different optical ports, i.e., sun port, nadir port, and calibration port yield the same spectral calibration data and spectral slit function calibration data. The positions of the spectral lines are known to an accuracy of better than 0.01 pixel, but the final accuracy of the spectral calibration is reduced by the effects mentioned above. For this reason the echelle slit function optical stimulus, which is discussed in detail in Section IX, was used via the calibration port in addition to the spectral lamp. The echelle optical stimulus is a grating used at high order coupled with a spectrally broad source. It outputs a set of spectral lines, for which the wavelength spacing is accurately known. Furthermore, the spectral lines have full widths at half maximum that are typically an order of magnitude lower than the OMI wavelength resolution, thus providing basically delta inputs to the OMI instrument in the wavelength dimension. This ensures that the response function as measured by the OMI instrument is dominated by the spectral slit function of the OMI instrument rather than the optical stimulus. The wavelength spacings between the stimulus spectral lines are almost independent of the exact angle of the echelle grating, in contrast to the absolute wavelengths of the lines, which are determined by the grating angle. The wavelength calibration of the OMI instrument is given by

$$\lambda_{ij} = \sum_{k=0}^{N} c_{kj} \cdot i^k \tag{1}$$

where i is the column number, j the row number, and c_{kj} are the wavelength calibration polynomial coefficients. N is the order of the polynomial, which is typically 4 for the UV1, UV2, and VIS subchannels. Using the echelle slit function optical stimulus allows for a very accurate determination of all c_{kj}, except the zero-order coefficient c_{oj}, which depends on knowledge of the absolute wavelengths of the optical stimulus spectral lines. These absolute wavelengths are not known *a priori*. By comparing the measurement results of the spectral lamp and the echelle optical stimulus the remaining c_{oj} parameters have been calibrated accurately as well. The accuracy of the on-ground wavelength calibration is about 0.1 pixel.

The in-flight spectral calibration is applied by the 0–1 data processor to Earth and sun measurements. Per subchannel a

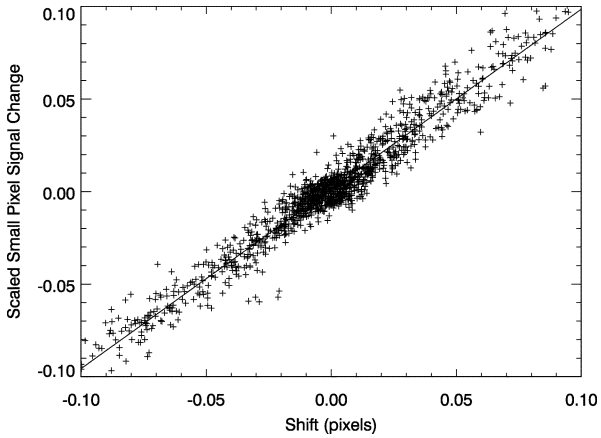

Fig. 39. Correlation for Earth shine spectra between wavelength shifts close to cloud transitions and gradients in small pixel column readouts for the VIS channel. This effect is attributed to partial slit illumination at inhomogeneous ground scenes and is corrected in the 0–1 data processor using a correlation as shown. In the figure the correlation coefficient is 0.96, and the slope is 0.92.

number of fitting windows are defined. In each window the measured spectrum is compared and fitted to a high-resolution literature solar spectrum [15] convolved with the accurately calibrated spectral slit function (Section IX). The nonlinear fitting process determines the wavelength scale of the window by shifting and squeezing the measured spectrum until an optimal match is obtained, for the Earth spectra ozone absorption and the atmospheric Ring effect are also taken into account. Subsequently, a polynomial (typically of order 4) is fitted through this set of predefined and optimized windows per subchannel. This defines the wavelength calibration per subchannel and per row. This algorithm is performed for each binned or unbinned row available in the measurement. Typical accuracies of the wavelength calibration that are obtained using the above algorithm on in-flight measurement data are for the solar spectra about 0.02 pixels in UV1, UV2, and VIS and for the Earth spectra 0.04–0.05 pixels in UV1, UV2, and VIS.

The results of the in-flight wavelength calibration on Earth spectra along complete orbits show that wavelength shifts of several hundredths of a pixel occur when the signal intensity changes, i.e., when ground scene changes in the flight direction occur, for example in case of clouds. This holds particularly for the UV2 and VIS channel, but not for the UV1 channel, because for wavelengths below 305 nm the ground is not seen and scene-to-scene variability is much less. The effect can be explained in terms of partial or nonuniform filling of the entrance slit in the flight direction, which is also the spectral dispersion direction. This influences the shape of the spectral slit function, which is narrowed and shifted with respect to the situation corresponding to complete uniform entrance slit filling. It turns out that it is possible to correct for this effect, which is the main contributor to the inaccuracies as quoted in the previous section, by using the small-pixel column data in the UV or VIS channel, for which a number of data points equaling the coadding factor are available for each read-out of the CCD detectors. The correction for this wavelength shift makes use of the correlation that exists between the observed wavelength shifts and the gradients in the small-pixel column data. Fig. 39 shows an example of this correlation in the VIS channel for an arbitrary orbit. By applying the wavelength correction for changing scenes the accuracy of the in-flight wavelength calibration of Earth shine spectra approaches 0.01 pixels, which is the goal accuracy for the in-flight wavelength calibration.

IX. Spectral Slit Function

The spectral slit function, which determines the measured spectral width (resolution) of the (ir)radiances spectral structures, was measured on the ground with the OMI instrument under flight-representative conditions. Since the slit function is different for every detector pixel, its determination is of critical importance for DOAS based retrieval of data products for which spectral shapes must be accurately determined.

In order to accurately measure the spectral slit functions a dedicated optical stimulus was designed that utilizes an echelle grating to produce an output beam containing about 50 spectral peaks in the wavelength range 264–504 nm, corresponding to the large number of diffraction orders of the echelle grating. These peaks are spectrally well separated and about ten times narrower in spectral width than the spectral resolution of the OMI instrument as listed in Table I. By rotating the echelle grating, the spectral peaks move in wavelength space and thus on the OMI CCD detector. The response of a detector pixel to a passing echelle peak yields the spectral slit function of that pixel. Rotation of the echelle grating gives the shape of the spectral slit function, which is measured with better sampling and at higher accuracy than is obtained using a spectral line source, for which the accuracy is limited by the pixel sampling of the spectral resolution by the detector. As listed in Table I, the ratio of the OMI spectral resolution to the pixel sampling typically is 3, whereas in the slit function measurements using the echelle optical stimulus ten times better sampling of the spectral resolution is achieved. For the OMI instrument the spectral slit function depends on wavelength, viewing direction, and the temperature of the optical bench (264 K).

The light beam of the echelle stimulus was coupled into the OMI instrument using the calibration port (via C08-C10 in Fig. 1), with the complete entrance slit 008 and thereby all CCD-rows (viewing angles) illuminated.

The advantage of moving an echelle spectral line over a fixed pixel is seen in Fig. 40. The upper plot shows the sampling of the spectral slit function when recording the response to the echelle slit function optical stimulus at a single echelle angle while the lower plot shows the improved sampling of the slit function measured using the dedicated echelle optical stimulus at multiple echelle angles. The solid line in both plots is a parameterized fit through the data points of the lower plot. Note that the solid line in the upper plot is not a fit through the small number of data points. For the UV1 spectral channel a standard Gaussian line shape was fitted, for the UV2 and VIS spectral channels a modified, broadened Gaussian profile was used. The functional parameterization describing the broadened Gaussian profile is

$$A_0 e^{-\left(\frac{x-x_0}{w_0}\right)^2} + A_1 e^{-\left(\frac{x-x_1}{w_1}\right)^4} \tag{2}$$

where A_0, A_1, x_0, x_1, w_0, w_1 are fitting parameters describing the amplitudes, positions, and widths, respectively. Note that x_0 and x_1 can be different, resulting in asymmetric slit function

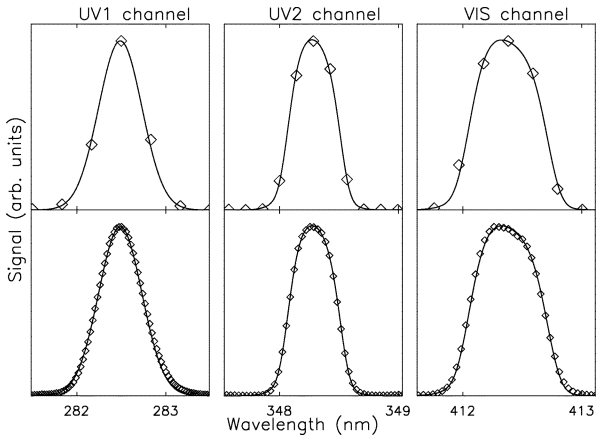

Fig. 40. OMI spectral slit function profile for each spectral channel. The upper panel presents the OMI response to a single narrow wavelength corresponding to a single echelle angle measurement and clearly shows the limited sampling of the spectral resolution of the instrument when illuminated with a spectral line. The lower panel presents the OMI slit function calibrated with the dedicated optical stimulus at multiple echelle angles; much better sampling is achieved with this stimulus, which moves the spectral feature in pixel space as the echelle grating is rotated. The solid line is a parameterized fit through the data: a Gaussian profile in UV1, a modified (broadened) Gaussian profile in UV2 and VIS. The fit result of the lower panel is coplotted in the upper panel for reference.

shapes, which have indeed been measured for certain ranges of CCD pixels. These results show that with the use of the echelle grating optical stimulus much more accurate calibration parameters for the spectral slit function can be obtained as compared to the use of single spectral lines.

X. In-Flight Detector Dark Signals

On-ground testing has shown that proton damage to the OMI CCD detectors can increase the dark current behavior of the individual CCD pixels in both the image and the storage sections. Proton-induced damage effects on CCDs are well-described in the literature [16], [17]. The dark current at 265 K is in the UV channel image area about 47 e/s per unbinned pixel (68 e/s in the storage area) and in the VIS channel image area about 86 e/s per unbinned pixel (91 e/s in the storage area). After single proton hits these initial dark current values roughly double on average. In order to minimize the damage, 10-kg additional aluminum shielding was added to shield the detector modules and CCD detectors. Furthermore, the operational temperature of the CCD detectors was lowered from about 278 to 265 K in order to minimize the impact of the radiation damage and the dark current increase. The temperature of the optical bench was also lowered from about 277 to 264 K. The average thickness of the additional aluminum shielding is about 29 mm. The location of the shielding is shown in Fig. 41. In this section the CCD detector performance during the first 200 days after launch is investigated.

Once per day the CCD detectors are read out in unbinned mode on the eclipse side of the orbit with the folding mirror C03 blocking the optical light path. These measurements are particularly well suited to determine dark currents of the individual pixels. The average dark signal is about 1700 binary units, but outliers with higher signals can be clearly identified. A similar analysis at the beginning of the mission or preflight

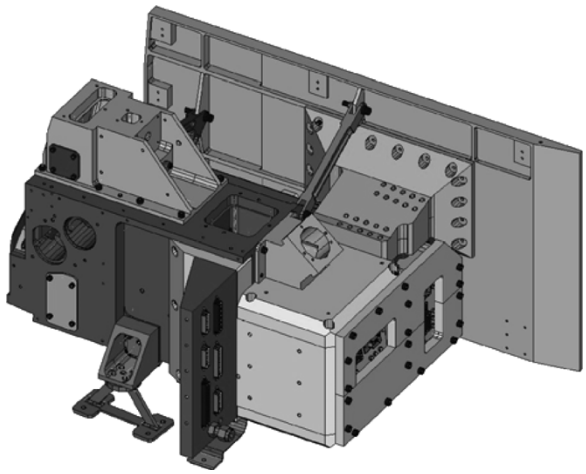

Fig. 41. OMI optical bench. The main radiator plate for cooling down the optical bench is located at the back. On the right-front and right side the additional 10-kg aluminum detector module shielding can be seen.

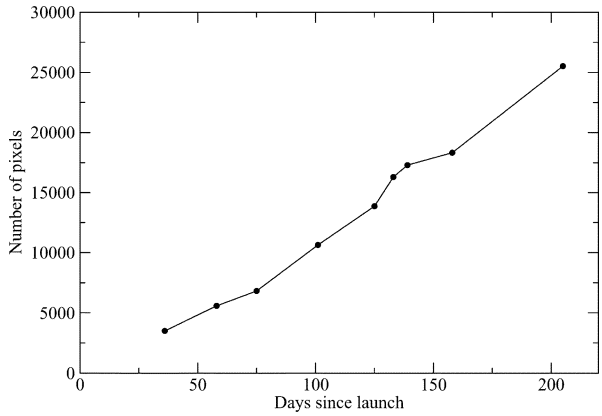

Fig. 42. Number of pixels with increased dark current as a function of time after launch for the UV CCD detector.

shows no such peaks with higher signals. The peaks of the individual pixels originate from an increase in dark signal after the pixel was hit by a damaging particle, most likely a proton. The observed peaks cannot be attributed to single events, such as the ones observed when the instrument passes though the South Atlantic Anomaly (SAA). In such cases increased activity is observed on the CCD images, but the increased signals disappear once the spacecraft leaves the SAA. An example of such increased temporary activity SAA behavior is shown in Fig. 43. In contrast, the peaks with lasting high dark signals represent a permanent increase in dark current resulting from damage to the CCD pixel in the form of lattice displacements. The behavior of the peaks has been investigated using a threshold algorithm to identify the pixels with increased signal. By examining multiple adjacent read-outs the single-event peaks are discarded and only the pixels that show a permanent high signal are taken into account. Fig. 42 shows the number of pixels with increased dark signal as a function of time after launch for the image areas of the UV CCD detector. It can be seen that the number of pixels with higher dark signals increases about linearly with time and that the line extrapolates more or less through zero at launch, as expected. The behavior for the VIS detector is almost identical.

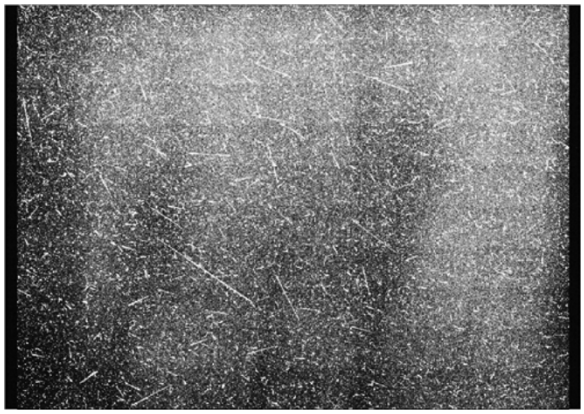

Fig. 43. Dark signal measurement with exposure time 136 s and gain factor 40 in SAA. The increased number of random hits and trails of particles can be observed.

Another way to visualize the changes in the CCD detector dark signal is to investigate the CCD histograms of the dark measurements. Fig. 44 shows such histograms for two measurements with exposure times of 36 s and gain factor 40 obtained on August 20, 2004 and February 5, 2005. It can be observed that the tail of the distribution toward higher signals increases with time. This behavior is known from and consistent with on-ground radiation testing with protons.

Proton radiation damage on CCD detectors is known from literature to cause a phenomenon known as random telegraph signal (RTS) [18], [19]. RTS in dark signal measurements manifests itself as a type of behavior where the output of a pixel is unstable and shows evidence for jumps between multiple more or less stable energy levels. This is a statistical process and the time constants of such jumps can vary per pixel. The exact times when an energy transition will occur cannot be predicted. It is known from literature that the time constants between jumps become longer when the CCD temperature is lowered. This behavior as known from literature has been confirmed on proton irradiated CCD samples before launch for the OMI instrument. Figs. 45–47 show for three individual pixels the time histograms (left) and dark currents (right) as a function of time. In these three cases it concerns pixels that were hit by a proton in the period November 25 to December 1, 2004. Before being hit these pixels behaved normally and as expected, i.e., with one dark current level and expected noise behavior with an occasional spike that causes no permanent damage. Fig. 45 shows an example of a pixel that was hit twice in one week, but still behaves normally, albeit with higher dark current. Fig. 46 shows an example of a pixel that shows regular RTS after being hit, at 2–3 energy levels, as confirmed by the histogram on the left. Fig. 47 shows an example of a pixel that shows erratic RTS behavior after being hit, with multiple energy levels or maybe even with a continuum of energy levels (see the histogram to the left). Fortunately, the latter category of RTS pixels (after proton hits) are a minority, with most pixels behaving as exemplified in Figs. 45 and 46 after being hit by a particle.

An interesting question is which particles are responsible for the dark current increase and CCD detector damage. In order to answer this question, the dedicated dark current measurements from November 25 to December 1, 2004 have

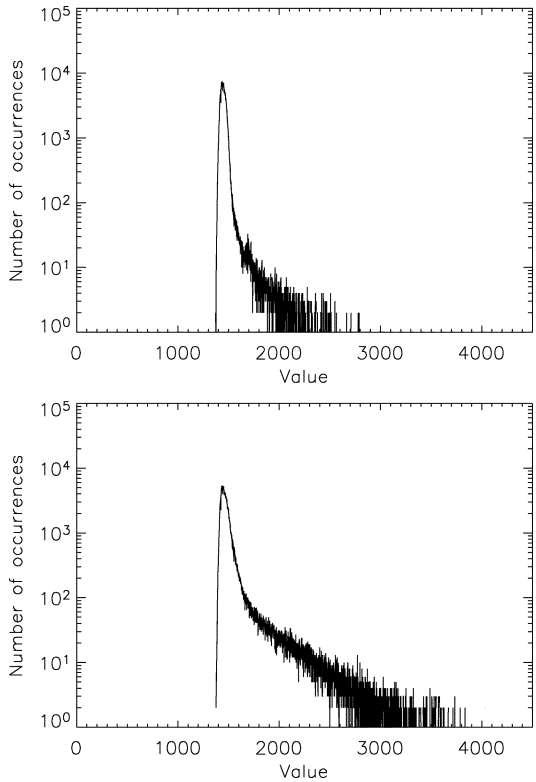

Fig. 44. Histograms of dark signal measurements (top) on August 20, 2004 and (bottom) February 5, 2005.

been investigated. During this period, for about 700 pixels on each detector the dark current has been observed to increase considerably, i.e., these pixels have been hit by a particle. The geolocation at which this increase occurred is shown in Fig. 48. It can be clearly seen that most damage occurs in the SAA and the radiation belts at the poles. This suggests that particles trapped in the Earth's magnetic field rather than free or direct solar particles are responsible for the observed phenomena. Trapped electrons can be ruled out, because they would not be able to penetrate the 29-mm-thick aluminum shielding. This leaves trapped protons as the most likely candidate for the CCD detector damage. Comparing the SAA area where most damage occurs according to our results to model calculations (ESA/SPENVIS) suggests that trapped protons with energies of more than about 10 MeV are the main origin for the observed damage. Fig. 49 shows the predicted end-of-life proton dose as a function of shielding thickness. It can be seen that, although the 29-mm-thick shielding stops about two thirds of the amount of protons, considerable amounts of protons are still able to reach the CCD detectors. The fact that so many particles reach the detectors despite the 29-mm-thick aluminum shielding provides further support to the assumptions that protons cause the observed damage. To what extent secondary particles originating in the aluminum shielding itself are contributing to the observed behavior is unknown. The nature of the damage in increased dark current and RTS behavior suggests that nonionizing energy loss damage is considerably more important than ionizing energy loss. The latter is known to be more capable of self-healing than the former.

Pixels that are hit by protons can still be used if Earth spectra are dark signal corrected with measurements that are obtained

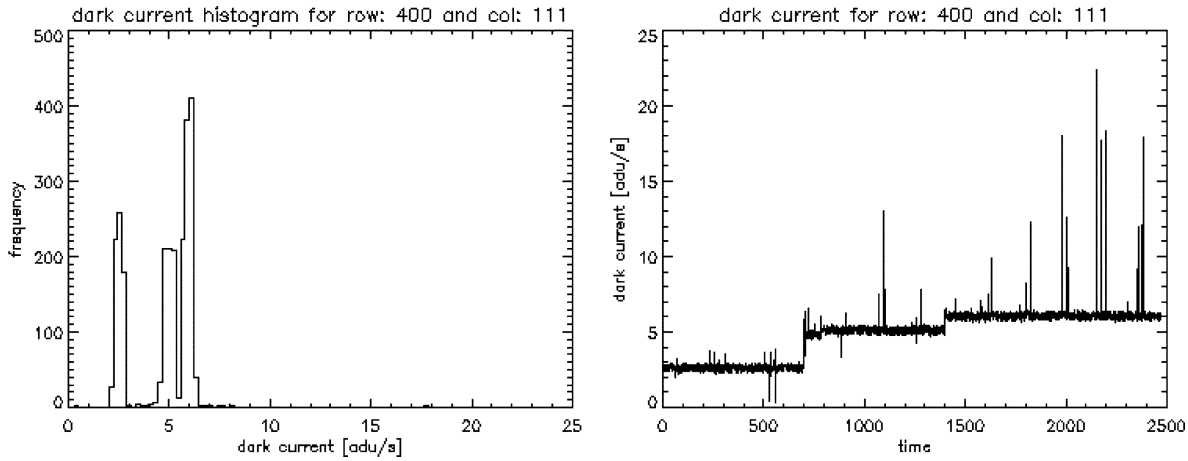

Fig. 45. Time histogram (left) and dark current as a function of time for the pixel at row 400 and column 111 in the UV channel. The pixel was hit twice in a period of one week, but for this pixel these hits do not cause RTS behavior.

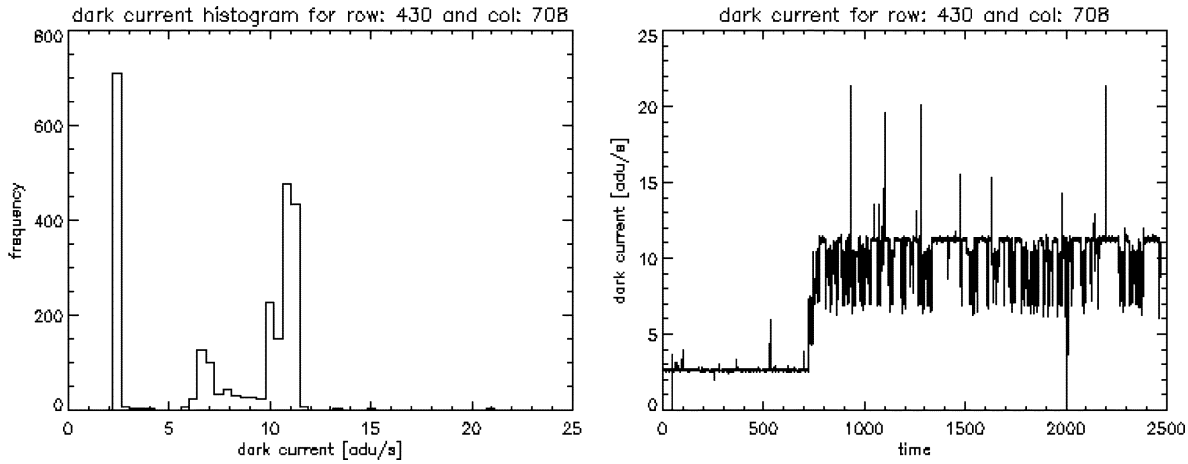

Fig. 46. Time histogram (left) and dark current as a function of time for the pixel at row 430 and column 708 in the UV channel. After being hit the pixel shows more or less regular RTS behavior, which was absent before the hit.

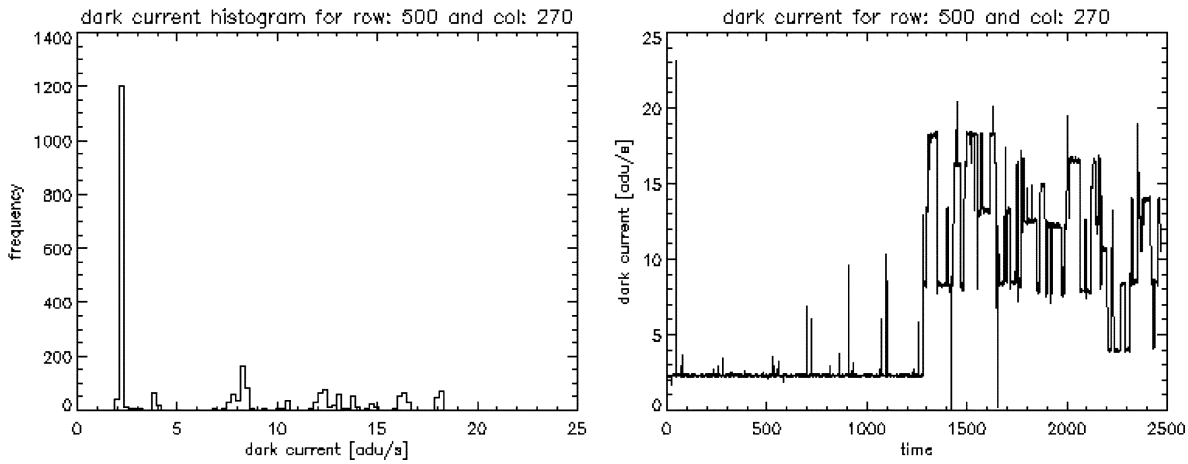

Fig. 47. Time histogram (left) and dark current as a function of time for the pixel at row 500 and column 270 in the UV channel. After being hit the pixel shows erratic RTS behavior, which was absent before the hit.

close in time to the light measurement, i.e., when the dark signal correction is sufficiently dynamic. Such a dynamic dark signal correction scheme is compromised if the pixels show significant RTS behavior. As explained above, nearly all pixels that have been hit by a proton show RTS behavior of some kind after the radiation damage. The exact appearance of the RTS behavior varies greatly between pixels. From inspection of the pixels with increased dark current it is estimated that about 95% of these pixels can still be used well for measurement purposes, because the dark signal can be corrected for using a dynamic dark signal

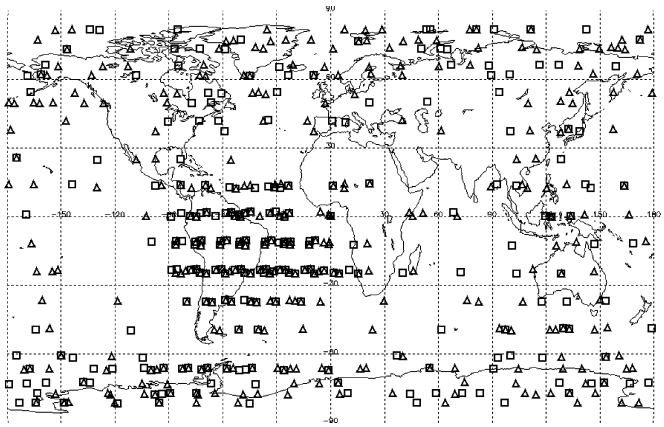

Fig. 48. Geolocations at which CCD detector pixels were hit resulting in increased dark current in the UV channel (triangles) and in the VIS channel (squares) in the time period November 25 to December 1, 2004. The South Atlantic Anomaly can be clearly identified.

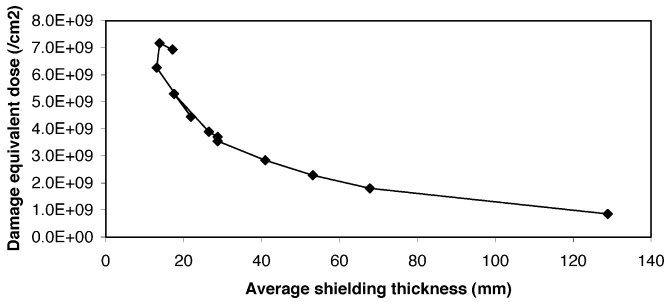

Fig. 49. Damage equivalent proton dose at the end of life as a function of aluminum shielding thickness. The average thickness used for OMI is 29 mm.

correction scheme. The remaining 5% shows damage to an extent that the pixel contents may be unreliable or inaccurate, because the dark current and/or noise shows large variations in time. In order to properly appreciate the impact of the CCD pixel proton radiation damage manifested by the increased dark current and RTS behavior one must realize that the results shown so far have been obtained with measurements with exposure times of 136 s and gain factor 40. Typical Earth-shine and sun measurements are performed with exposure times of 0.5–1.0 s and gain factors of 4 or 10, i.e., the impact of the proton damage on actual Earth or sun measurements is typically three orders of magnitude smaller than discussed above. Furthermore, the Earth and sun measurements are performed with electronic binning factor four or eight, whereas the long dark measurements shown above have been performed with binning factor one. So even when the proton radiation damage on the CCD detectors is a compromising factor for the quality of the Earth and sun measurements and the exact impact of the damage must be continuously monitored, the impact on the OMI science data is not as severe as might have been suggested by the results shown in this section, which present extreme cases obtained with extreme measurement settings that are not at all representative for the regular OMI science measurements. In order to be able to deal properly with the pixel-dependent varying dark currents of the CCD detectors in the 0–1 data processing a dynamic dark signal correction scheme that is able to use the appropriate dark signal measurements close in time to the Earth and sun measurements is currently in preparation.

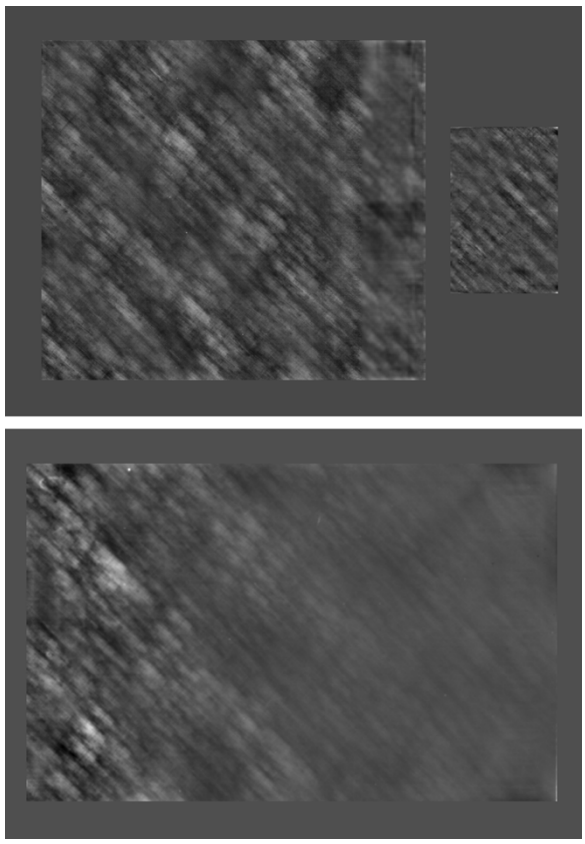

Fig. 50. PRNU for (top) UV channel (left, UV2 and right, UV1) and (bottom) VIS channel.

XI. Detector Pixel Response Nonuniformity

The PRNU is a detector property that describes the relative response of each individual pixel. If not corrected properly, PRNU introduces high-frequency instrument-related structures in the calibrated measurement data. The PRNU is strongly wavelength dependent, because at higher wavelengths the penetration depth of the photons in the silicon material is smaller. For the OMI wavelength range 264–504 nm the PRNU has a typical peak-peak amplitude of about 5% at the shorter wavelength end and decreases gradually to a peak-peak amplitude of typically 0.1% at 500 nm. Although PRNU is dependent on the wavelength, the effect is purely CCD detector related. PRNU is caused by differences in individual pixel size and surface treatment. The PRNU for the CCD detectors used in OMI shows a diagonal pattern, as shown in Fig. 50.

In order to determine and calibrate the PRNU, the spectrometer has to be illuminated with a white light source which has no spectral output variation on a scale of more than 10^{-4} at the typical PRNU periods in the wavelength and viewing dimensions as shown in Fig. 50. This so-called flat-fielding is in practice more easily said than done. Usually an irradiance source illuminates a diffuser, for example one of the three internal OMI reflectance diffusers, an external spectralon diffuser, or the internal OMI transmission diffuser. As explained earlier, the OMI aluminum diffusers introduce spectral and spatial features on a 10% scale (see Sections III-C and V-D). An external spectralon reflectance diffuser also introduces spectral features on a 10^{-3} scale and furthermore it is not possible to illuminate the

complete image area on the CCD detectors instantaneously. The internal OMI WLS illuminates the OMI transmission diffuser C05, which also introduces diffuser features on a 1% scale, as shown in Section III. For these reasons, it was decided to determine the prelaunch PRNU from irradiance measurements over the quartz volume diffuser, which results in the smallest possible features, and from the internal WLS over the transmission diffuser C05. The latter option was examined despite the features introduced by the transmission diffuser, because it is the most promising option to be used in flight. By comparing the two light sources it has been possible to identify the transmission diffuser contribution as shown earlier in Fig. 6. The irregularities of the entrance slit 008, shown earlier in Fig. 5, influence the accuracy of the PRNU calibration. In flight the PRNU is verified and may be adjusted when necessary using the unbinned internal WLS measurement data, which are measured once per week. Note that the PRNU is equal for the radiance and irradiance modes and for this reason cancels in zero order in the ratio of the two, i.e., in the Earth reflectances.

XII. Detector Nonlinearity

Light flux is converted to collected charge in the CCD pixels, which is in turn clocked on the on-chip preamplifier with potential use of binning in the readout register. The (amplified) analog signals are fed into the ELU, where they are digitized. On-ground testing revealed that the DEM amplifier is the dominant source for the OMI system nonlinearity (signal-dependent gain).

On the ground the nonlinearity has been measured on DEM unit level as well as on integrated OMI system level at flight-representative conditions using combinations of variation of the detector exposure times and variation of the light fluxes offered to the instrument. For the latter tests a dedicated optical stimulus equipped with accurately calibrated neutral-density filters and output-flux monitoring has been used. For the former tests both the dedicated optical stimulus and the OMI internal white light source have been used. The WLS results are not the most accurate ones, but they can be used as a reference for in-flight nonlinearity analyses. The results on unit level and on instrument level were found to be consistent.

Fig. 51 shows the deviation from linear behavior of the integrated OMI system. The figure shows the relative errors as a percentage of the number of electrons in the reference signal. Nonlinear behavior is significant above 10^5 electrons. Readout register full well saturation is observed to occur at $2 \cdot 10^6$ electrons. The nonlinearity, which can be up to 3.5%, is corrected in the 0–1 software to better than 0.1%. In flight the nonlinearity can be studied with dedicated white light source and LED measurements in which the exposure times are varied.

An estimate of response linearity at the high end of the dynamic range can also be obtained using the UV2 and VIS channel overlap region. Large sensitivity differences exists between these two channels for radiances between 350 and 380 nm. Radiances at 366 nm remain in the linear range of the UV2 detector while the same radiances push the VIS detector into the nonlinear regime and even to saturation. It was verified that the ratio of radiances measured in the two channels is constant, indicating that nonlinearities are properly corrected in the 0–1 processing.

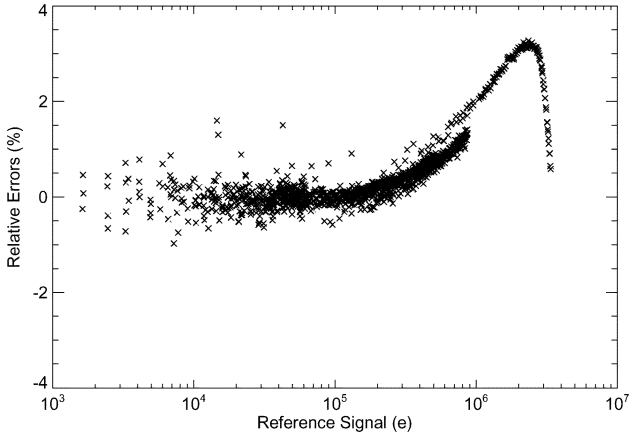

Fig. 51. OMI system deviation to linear behavior. The figure shows the relative error as a percentage of the number of electrons in the reference signal.

XIII. Conclusion

The optical and electrical design of the Ozone Monitoring Instrument, successfully launched on July 15, 2004 on the EOS Aura satellite, has been described in detail. A number of important performance and calibration results as measured on the ground have been presented and discussed, as well as a selection of in-flight results. The OMI instrument works flawlessly, and the in-flight performance is as expected from on-ground testing. The results show that the radiometric calibration in comparison to the high-resolution literature solar irradiance spectrum convolved with the measured spectral slit function is understood and as expected in terms of offsets and spectral structure. The in-flight wavelength calibration and assignment is close to the required accuracy of about 0.01 pixel. The instrument shows no signs of optical degradation over the wavelength range 264–504 nm over the first seven months after launch. The in-flight performance of both CCD detectors shows evidence of particle hits of trapped high-energetic protons. The resulting detector performance changes can be to a large extent corrected for by a dynamical dark signal correction scheme in the 0–1 data processing, which is in preparation. More detailed analysis work on the available in-flight measurement data is required to fully understand the in-flight calibration and performance behavior of the OMI instrument and to improve the quality of the L1 measurement data further. From the on-ground and in-flight results presented in this paper, OMI is expected to meet its key mission objectives.

References

[1] P. F. Levelt, E. Hilsenrath, G. W. Leppelmeier, G. H. J. van den Oord, P. K. Bhartia, J. Tamminen, J. F. de Haan, and J. P. Veefkind, "Science objectives of the Ozone Monitoring Instrument," *IEEE Trans. Geosci. Remote Sens.*, vol. 44, no. 5, pp. 1199–1208, May 2006.

[2] R. D. McPeters, P. K. Bhartia, J. K. Arlin, J. R. Herman, C. G. Wellemeyer, C. J. Seftor, G. Jaross, O. Torres, L. Moy, G. Labow, W. Byerly, S. L. Taylor, T. Swissler, and R. P. Cebula, Earth probe Total Ozone Mapping Spectrometer (TOMS) Data Products User's Guide, NASA Goddard Space Flight Center, Greenbelt, MD, 1998.

[3] U. Platt, "Differential Optical Absorption Spectroscopy (DOAS)," in *Air Monitoring by Spectroscopic Technique*, M. W. Sigrist, Ed. New York: Wiley, 1994, pp. 27–84.
[4] J. M. C. Plane and N. Smith, "Atmospheric monitoring by differential optical absorption spectroscopy in environmental science," in *Adv. Spectrosc.*, 1994, vol. 24.
[5] J. P. Veefkind, J. F. de Haan, E. J. Brinksma, M. Kroon, and P. F. Levelt, "Total ozone from the Ozone Monitoring Instrument (OMI) using the DOAS Technique," *IEEE Trans. Geosci. Remote Sens.*, vol. 44, no. 5, pp. 1239–1244, May 2006.
[6] P. F. Levelt, G. H. J. van den Oord, M. R. Dobber, J. Claas, H. Visser, and J. de Vries, "The Ozone Monitoring Instrument," *IEEE Trans. Geosci. Remote Sens.*, vol. 44, no. 5, pp. 1093–1101, May 2006.
[7] R. Dirksen, M. Dobber, P. Levelt, G. H. J. van den Oord, G. Jaross, M. Kowalewski, G. H. Mount, D. Heath, E. Hilsenrath, and J. de Vries, "The on-ground calibration of the Ozone Monitoring Instrument from a scientific point of view," in *Proc. SPIE 10th Int. Symp. Remote Sensing*, vol. 5234, Barcelona, Spain, Sep. 8–12, 2003, pp. 400–410.
[8] M. Dobber, R. Dirksen, P. F. Levelt, G. H. J. van den Oord, G. Jaross, M. Kowalewski, G. H. Mount, D. Heath, E. Hilsenrath, and R. Cebula, "Ozone Monitoring Instrument flight-model on-ground and in-flight calibration," presented at the *Int. Conf. Space Optics (ICSO)*, Toulouse, France, 30 Mar.–2 Apr., 2004.
[9] J. de Vries, G. H. J. van den Oord, E. Hilsenrath, M. te Plate, P. Levelt, and R. Dirksen, "Ozone Monitoring Instrument (OMI)," in *Proc. SPIE Conf. Imaging Spectrometry VII*, vol. 4480, M. R. Descour and S. S. Chen, Eds., San Diego, CA, Aug. 1–3, 2001, pp. 315–325.
[10] G. H. J. van den Oord, J. P. Veefkind, P. F. Levelt, and M. R. Dobber, "OMI Level 0 to 1B processing and operational aspects," *IEEE Trans. Geosci. Remote Sens.*, vol. 44, no. 5, pp. 1380–1397, May 2006.
[11] J. J. Butler, H. Park, Y. P. Barnes, E. A. Early, C. van Eijk-Olij, A. E. Zoutman, S. Buller-van Leeuwen, and J. G. Schaarsberg, "Comparison of ultraviolet bidirectional reflectance distribution function (BRDF) measurements of diffusers used in the calibration of the Total Ozone Mapping Spectrometer (TOMS)," in *Proc. SPIE*, vol. 4881, 2002, pp. 345–354.
[12] G. Jaross, A. J. Krueger, and D. Flittner, "Multispectral calibration of remote-sensing instruments over Antarctica," *Metrologia*, vol. 35, pp. 625–629, 1998.
[13] G. Jaross, R. D. McPeters, P. K. Bhartia, D. P. Haffner, S. L. Taylor, and C. G. Wellemeyer, "Earth probe TOMS optical degradation and calibration corrections," in *Proc. 20th Quad. Ozone Symp. 2004*, C. S. Zerefos, Ed., Athens, Greece, 2004, pp. 546–547.
[14] T. C. Grenfell, S. G. Warren, and P. C. Mullen, "Reflection of solar radiation by the Antarctic snow surface at ultraviolet, visible, and near-infrared wavelengths," *J. Geophys. Res.*, vol. 99, pp. 18 669–18 684, 1994.
[15] R. L. Kurucz, I. Furenlid, J. Brault, and L. Testerman, *Solar Flux Atlas From 296 to 1300 nm*. Sunspot, NM: Nat. Solar Observ., 1984.
[16] C. Date, "Displacement damage effects in mixed particle environments for shielded spacecraft CCD's," *IEEE Trans. Nucl. Sci.*, vol. 40, no. 6, pp. 1628–1637, Dec. 1993.
[17] M. S. Robbins, "High energy proton-induced dark signal in silicon charge coupled devices," *IEEE Trans. Nucl. Sci.*, vol. 47, no. 6, pp. 2473–2479, Dec. 2000.
[18] I. H. Hopkins and G. R. Hopkinson, "Random telegraph signals from proton-irradiated CCD's," *IEEE Trans. Nucl. Sci.*, vol. 40, no. 6, pp. 1567–1574, Dec. 1993.
[19] ——, "Further measurements on random telegraph signals in proton-irradiated CCD's," *IEEE Trans. Nucl. Sci.*, vol. 42, no. 6, pp. 2074–2081, Dec. 1995.

Marcel R. Dobber studied experimental physics from 1990 to 1994 at the Free University of Amsterdam, Amsterdam, The Netherlands, and received the Ph.D. degree in physical chemistry from the University of Amsterdam, for work on high-resolution and time-resolved molecular laser spectroscopy.

He started working on Earth observation from space in 1995 and joined the Royal Dutch Meteorological Institute (KNMI), De Bilt, The Netherlands, in 2001, where he has been working mainly on the development and on-ground and in-flight calibration of the OMI instrument on NASA's EOS Aura satellite.

Ruud J. Dirksen received the masters degree in physics from the University of Amsterdam, Amsterdam, The Netherlands, in 1994.

After working in the field of semiconductor research for a couple of years, he joined the OMI team in 2000 and has been involved in the calibration of the instrument since then.

Pieternel F. Levelt received the M.S. degree in physical chemistry and the Ph.D. degree from the Free University of Amsterdam, Amsterdam, The Netherlands, in 1987 and 1992, respectively. Her Ph.D. work consisted of the development of a XUV spectrometer-based nonlinear optical technique and performing XUV spectroscopy on small diatomic molecules.

In 1993, she started working at the Royal Netherlands Meteorological Institute (KNMI), De Bilt, in the Atmospheric Composition section at the Research Department of KNMI. There, she worked on chemical data assimilation of ozone in two-dimensional and three-dimensional chemistry transport models and on the validation of the European satellite instruments GOME and SCIAMACHY. She was a Member of the Algorithm and Validation subgroups of GOME and SCIAMACHY. She was strongly involved in the validation program of both instruments. Since July 1998, she has been Principal Investigator of the OMI instrument and is responsible for the scientific program of OMI and managing the international OMI Science Team. She is also the Project Manager of the OMI Program at KNMI and responsible for the development of algorithms, validation, and data processing of OMI products and in-flight calibration and operational planning of the OMI instrument. She is managing the OMI team at KNMI consisting of 15 to 35 people. As Principal Investigator, she is advising NIVR on OMI instrument requirements and performance.

G. H. J. van den Oord is currently with the Royal Dutch Meteorological Institute (KNMI), De Bilt, The Netherlands. He has a 16-year-long background in both observational and theoretical astrophysics with emphasis on solar and stellar magnetic activity. On the theoretical side, he has worked in the fields of magnetohydrodynamics, plasma physics, beam electrodynamics, high-energy astrophysics, X-ray spectroscopy, and radiative transport. On the observational side, he has been an active user of (ground-based) radio and optical instrumentation, and spaceborne X-ray and (E)UV instrumentation. He has supervised two Ph.D. students and is author and coauthor of 72 papers. Since April 1999, he has been the Deputy Principal Investigator of the Ozone Monitoring Instrument. He has been a Visiting Professor at the University of Catania. He has been a member of numerous science advisory boards on both national and international level.

Dr. van den Oord received an award from Utrecht University for outstanding research accomplishments.

Robert H. M. Voors received the M.Sc. degree in astrophysics and the Ph.D. degree from Utrecht University, Utrecht, The Netherlands, in 1994 and 1999, respectively. His Ph.D. thesis was for his study of the evolution of the most massive stars.

He went to work at the Royal Netherlands Meteorological Institute (KNMI), De Bilt, for the OMI project in 1999, first on the development of retrieval algorithms, and later on the in-flight calibration of OMI.

Quintus Kleipool received the Ph.D. degree on airborne submillimeter Earth observation and since then has worked on the detector calibration of the SCIAMACHY instrument on the European Space Agency ENVISAT satellite. In 2005, he joined the Royal Netherlands Meteorological Institute (KNMI), De Bilt, to assist with the detector calibration of the Ozone Monitoring Instrument.

Glen Jaross received the Ph.D. degree in high-energy particle physics from the University of Illinois at Urbana-Champaign, in 1990.

He has since been under contract with the NASA Goddard Space Fight Center, Greenbelt, MD, to provide sensor calibration and analysis support, and is currently employed by Science Systems and Applications, Inc., Lanham, MD. His primary expertise is in the calibration and monitoring of backscatter ultraviolet sensors, primarily used to measure atmospheric ozone.

Matthew Kowalewski received the B.S. degree in astronomy and physics from Boston University, Boston, MA, and the M.S degree in applied physics from the Johns Hopkins University, Baltimore, MD.

He is currently an Instrument Engineer for Science Systems and Applications, Inc., Lanham, MD, at the NASA Goddard Space Flight Center, Greenbelt, MD, supporting instrument design and calibration activities.

Ernest Hilsenrath was with NASA's Goddard Space Flight Center from 1965 to August 2005. He was Deputy Project Scientist for the EOS Aura mission and is Co-Principal Investigator for the Ozone Monitoring Instrument flying on Aura. In the 1970s, he developed a unique rocket payload to measure ozone profiles in the stratosphere and lower mesosphere. He also conducted ozone and water vapor measurements from rockets, balloons, and aircraft. He was the Principal Investigator of the Shuttle-borne SBUV instrument, flown eight times, to calibrate the SBUV/2 series of instruments in the NOAA polar orbiting satellites. He managed the Goddard Space Flight Center's Radiometric Calibration and Development Facility. The laboratory provides calibrations for national international satellite ozone instruments and developed the first UV/VIS limb scattering instruments to demonstrate, from the Space Shuttle, the ozone monitoring capability for NPOESS. He served on and chaired several international panels for atmospheric composition observations including NPOESS and Eumetsat. He is Chairman of the CEOS Cal/Val Working Group's Atmospheric Chemistry Subgroup. He has authored more than 50 papers on atmospheric composition and calibration/validation in peer-reviewed journals. He is currently a staff member at the University of Maryland Baltimore County, Baltimore, at the Joint Center for Earth Systems Technology.

Gilbert W. Leppelmeier (M'72) has been involved in space research missions for 19 years, first at the Technical Research Centre of Finland and then at the Finnish Meteorological Institute. He was Co-Principal Investigator for the Ozone Monitoring Instrument onboard Aura from the start of the mission through 2004. Other space missions include Envisat, Odin, SOHO, Spectrum-Roentgen-Gamma, Cassini/Huygens, as well as a number of studies of atmospheric missions to Mars and Earth. Earlier research includes solid-state physics, nonlinear optics, laser fusion energy, and magnetic fusion energy. Since retirement from FMI in 2000 his continued activity in space and atmospheric sciences has been under the aegis of G&S Associates, Oy, Espoo, Finland.

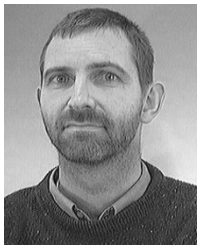

Johan de Vries has over 15 years of experience in developing spectrographs for space. He has acted as OMI Project Scientist on the industrial side from 1994 up to launch on EOS Aura in 2004. He is currently a Design Leader for future air quality instruments at Dutch Space BV, Leiden, The Netherlands.

Werner Dierssen received the M.Sc. degree in computer science from the University of Twente, Twente, The Netherlands.

He is currently working for TriOpSys BV, Maarssen, The Netherlands. He has been working as a Calibration Programmer on the OMI project since 2004.

Nico C. Rozemeijer received the B.Sc. degree in electrical engineering.

Since receiving his degree, he has worked as a Software Engineer on a broad range of projects. He is currently a Software Engineer with TriOpSys BV, Maarssen, The Netherlands, working on the OMI project since 2000.